Entrainment rates and microphysics in POST stratocumulus

H. Gerber,[1] G. Frick,[2] Szymon P. Malinowski,[3] H. Jonsson,[4] D. Khelif,[5] and Steven K. Krueger[6]

Received 12 February 2013; revised 2 August 2013; accepted 30 September 2013.

[1] An aircraft field study (POST; Physics of Stratocumulus Top) was conducted off the central California coast in July and August 2008 to deal with the known difficulty of measuring entrainment rates in the radiatively important stratocumulus (Sc) prevalent in that area. The Center for Interdisciplinary Remotely-Piloted Aircraft Studies Twin Otter research aircraft flew 15 quasi-Lagrangian flights in unbroken Sc and carried a full complement of probes including three high-data-rate probes: ultrafast temperature probe, particulate volume monitor probe, and gust probe. The probes' colocation near the nose of the Twin Otter permitted estimation of entrainment fluxes and rates with an in-cloud resolution of 1 m. Results include the following: Application of the conditional sampling variation of classical mixed layer theory for calculating the entrainment rate into cloud top for POST flights is shown to be inadequate for most of the Sc. Estimated rates resemble previous results after theory is modified to take into account both entrainment and evaporation at cloud top given the strong wind shear and mixing at cloud top. Entrainment rates show a tendency to decrease for large shear values, and the largest rates are for the smallest temperature jumps across the inversion. Measurements indirectly suggest that entrained parcels are primarily cooled by infrared flux divergence rather than cooling from droplet evaporation, while detrainment at cloud top causes droplet evaporation and cooling in the entrainment interface layer above cloud top.

Citation: Gerber, H., G. Frick, S. P. Malinowski, H. Jonsson, D. Khelif, and S. K. Krueger (2013), Entrainment rates and microphysics in POST stratocumulus, *J. Geophys. Res. Atmos.*, *118*, doi:10.1002/jgrd.50878.

1. Introduction

[2] Large sheets of stratocumulus clouds (Sc) along western margins of continents and under subtropical high-pressure regions strongly affect the radiation balance of the globe by reflecting visible solar radiation. It is thus necessary to understand the behavior of these Sc and to be able to predict their evolution in the future. An important physical process that can affect Sc dissipation is thought to be subsiding warm and dry air from above the mixed boundary layer that enters Sc cloud top causing cloud water to evaporate. This process is termed cloud top entrainment which has been the subject of numerous field studies of Sc off the western coasts of the American continents including the Marine Stratocumulus Experiment (MSE) [*Wakefield and Schubert*, 1976; *Gerber*, 1986], First International Satellite Cloud Climatology Project Regional Experiment (FIRE) [*Albrecht et al.*, 1988], Dynamics and Chemistry of Marine Stratocumulus (DYCOMS) [*Lenschow et al.*, 1988], East Pacific Investigation of Climate [*Bretherton et al.*, 2004], DYCOMS II [*Stevens et al.*, 2003a], and VAMOS Ocean-Cloud-Atmosphere-Land Study Regional Experiment (VOCALS) [*Wood et al.*, 2011]. A comprehensive review of Sc research is given by *Wood* [2012].

[3] In July and August 2008, another aircraft field study, POST (Physics of Stratocumulus Top) [*Gerber et al.*, 2010], used 17 flights off the California (CA) coast to again analyze entrainment in maritime Sc. POST was patterned after the DYCOMS II aircraft study [*Stevens et al.*, 2003a] conducted 7 years earlier that also focused on entrainment in unbroken Sc off the CA coast. Both studies dealt with our continuing inability to adequately measure and model entrainment; and both studies had goals to accurately measure entrainment velocity (w_e) into cloud top and use w_e as baseline data for comparison with model predictions. The desire to again study CA Sc during POST is a result of our learning from DYCOMS II that dimensions of entrainment parcels (also called "cloud holes") [*Korolev and Mazin*,

[1]Gerber Scientific, Inc., Reston, Virginia, USA.
[2]Naval Research Laboratory, Washington, D.C., USA.
[3]Institute of Geophysics, Faculty of Physics, University of Warsaw, Warsaw, Poland.
[4]Center for Interdisciplinary Remotely-Piloted Aircraft Studies, Naval Postgraduate School, Monterey, California, USA.
[5]Department of Mechanical and Aerospace Engineering, University of California, Irvine, California, USA.
[6]Department of Atmospheric Sciences, University of Utah, Salt Lake City, Utah, USA.

Corresponding author: H. Gerber, Gerber Scientific, Inc., 1643 Bentana Way, Reston, VA 20190, USA. (hgerber6@comcast.net)

2169-897X/13/10.1002/jgrd.50878

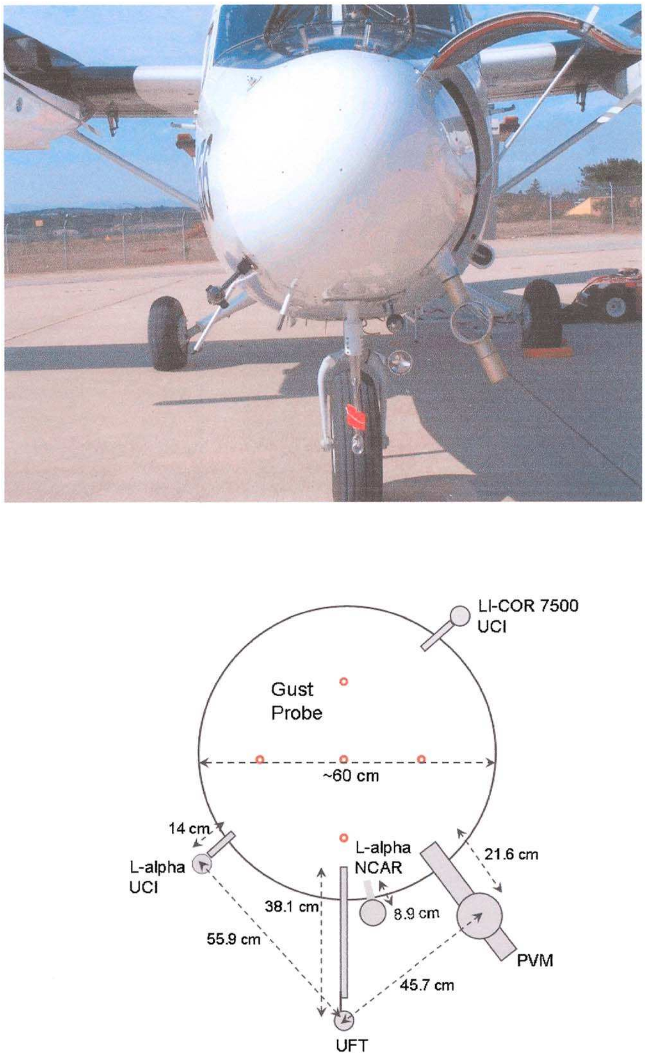

Figure 1. Head-on view of the CIRPAS Twin Otter (TO) research aircraft showing the locations of the UFT-M and PVM probes, and the Lyman-alpha probes which surround the UCI five-hole gust probe on the aircraft's nose.

1993] are relatively small [*Gerber et al.*, 2005], requiring fast and closely placed sensors on a research aircraft. In retrospect, excessive probe separation and slow probe response times likely contributed to the uncertainty of w_e measurements made by four independent techniques on the C-130 aircraft during DYCOMS II [*Gerber et al.*, 2005; *Faloona et al.*, 2005; *Haman et al.*, 2007]. The DYCOMS II w_e measurements differed by as much as a factor of 4 for each flight causing uncertainty in using w_e values for model comparison [*Stevens et al.*, 2003b].

[4] POST and DYCOMS II also differ in that the former study was located about 125 km off the coast near Monterey Bay, while the latter was located about 500 km SW of San Diego. POST is more closely related geographically to the earlier aircraft study "Marine Stratocumulus Experiment" (MSE) [*Wakefield and Schubert*, 1976] off the CA coast near San Francisco. While DYCOMS II was located far from the coastline to minimize continental effects on the Sc, both MSE and POST were located closer to the CA coastline in areas with strong sea surface temperature gradients that can cause a sloped CTBL (cloud topped boundary layer) with wind shear at cloud top due to the baroclinic nature of the atmosphere [*Brost et al.*, 1982a, 1982b; *Gerber et al.*, 1989]. It is suggested that wind shear affects entrainment [*Brost et al.*, 1982a, 1982b; *Moeng et al.*, 2005; *de Roode and Wang*, 2007; *Wang et al.*, 2008, 2012; *Katzwinkel et al.*, 2011].

[5] POST had the unique opportunity to investigate the vertical structure on either side of unbroken Sc top in unprecedented detail. This was possible by utilizing the CIRPAS (Center for Interdisciplinary Remotely-Piloted Aircraft Studies) Twin Otter (TO) research aircraft where probes pertinent to the entrainment process were mounted close to each other. This included the UFT-M (ultrafast temperature probe [*Kumula et al.*, 2013]; UFT-M is a modified version of the UFT described by *Haman et al.* [2001, 2007]) capable of 1000 Hz temperature (T) measurements in and out of cloud, the PVM (particle volume monitor) [*Gerber et al.*, 1994] also capable of 1000 Hz measurements of liquid water content (LWC) and droplet effective radius (R_e), and several probes for measuring the water vapor mixing ratio (q_v). Given the TO speed of ~50 m/s during cloud flights and the UFT-M and PVM ~0.5 m separation on the TO suggests that useful correlations between the UFT-M, PVM, and gust probe can be found at a 50 Hz rate corresponding to a horizontal in-cloud resolution of ~1 m. For a description of TO flights, flight scientist reports, and source of data, see the POST Web site at http://www.eol.ucar.edu/projects/post/. A list of TO instrumentation and their flight performance during POST are given in http://www.gerberscience.com/POSTdata/POSTdata.html.

[6] The high-resolution LWC measurements in POST flights make it possible as in *Gerber et al.* [2005] to use a "flux-jump" approach with "conditional sampling" to pick out cloud holes caused by entrainment near cloud top and to use the combination of LWC, T, and q_v data and the jump in the value of the scalar q_t (total water mixing ratio) across the inversion above cloud top to estimate entrainment fluxes and w_e. In the following, the inversion is given the alternate name EIL (entrainment interface layer; first observed and named using tethered balloons in continental Sc by *Chaughey et al.* [1982] and *Roach et al.* [1982] and in maritime Sc by *Gerber* [1986], and by *Lenschow et al.* [2000] in horizontal aircraft flight near Sc top).

[7] The w_e estimates also provide the opportunity to test three conditions thought to be necessary in classical mixed layer theory for applying the flux-jump approach to Sc using q_t as the scalar conserved during entrainment: Entrainment flux is linear with height below Sc top, entrained parcels are negatively buoyant and descend in Sc, and the jump in the value of q_t above Sc top is large and occurs over a thin layer.

[8] The high-resolution data further make it possible to investigate in detail individual cloud holes to clarify existing questions dealing with cooling contributions from LWC evaporation and IR flux divergence, with heating due to mixing with warmer air from above cloud top, with buoyancy reversal, with the relationship between entrained parcel scales and entrainment rates, and with the mixing mechanism following entrainment.

[9] The paper is organized into four sections. Section 2 includes a description of the TO instrumentation and of the aircraft flight patterns during the Sc missions and tabulates

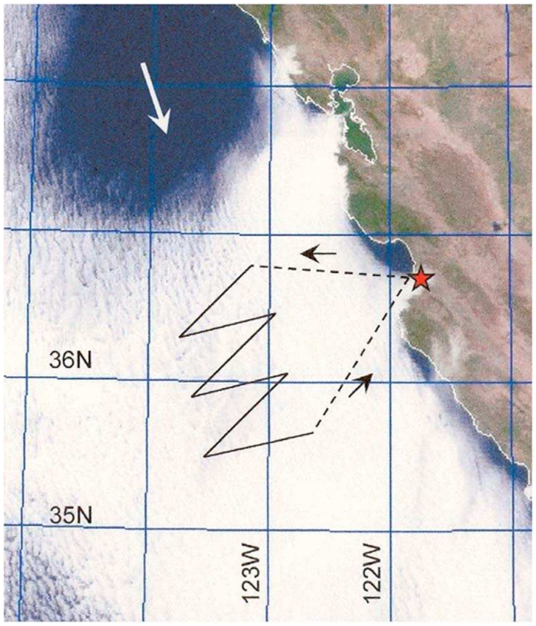

Figure 2. Early evening NexSat image (courtesy of the Naval Research Laboratory, Monterey) off the CA coast and the Pacific Ocean showing the approximate track of the Twin Otter aircraft on flight TO3 (19 July, UTC). The red star indicates the location of Marina airport near Monterey Bay, and the white arrow is the prevailing wind direction at cloud level. The Sc is dissipating upwind from the track.

data collected on each flight. Section 3 explains the method used for calculating entrainment velocities for all flights and analyzes in greater detail three off the flights. Section 4 looks at microphysics of the entrainment process including assessing the cooling effect at cloud top. Section 5 gives conclusions and makes recommendations for additional Sc research.

2. Observations

2.1. Instrumentation

[10] Instrumentation primarily dealt with in this study is located near the nose of the TO shown in the photo and dimensional sketch in Figure 1. Probes mounted on a hard-point ring near the gust probe on the nose include the UFT-M, PVM, and three probes for measuring q_v. This study relies in cloud-free air on relatively slow rate q_v data of several hertz from the University of California, Irvine (UCI)-modified LI-COR 7500 Lyman-alpha probe [*Khelif et al*., 2005] since the fast cross-flow UCI Lyman-alpha probe failed early in the field program, and since the fast National Center for Atmospheric Research (NCAR) Lyman-alpha probe produced noisy data. The gust probe consists of five holes leading to pressure transducers that produce after-correction for aircraft motions ambient wind speed and wind fluctuations at a data rate of 40 Hz and 50 Hz [*Khelif et al*., 1999].

[11] The TO also carried a full set of other instrumentation with a partial list including visible and IR radiometers mounted on the top and bottom of the fuselage for estimating radiation fluxes, Rosemount temperature probe, dewpoint hygrometer, particle and droplet spectrometers, cloud condensation nuclei counters, sea surface temperature probe, and GPS receiver for navigation and data time synchronization. The latter was used to produce 0.5 Hz square wave pulses to synchronize data collected by multiple data loggers and computers on board the aircraft. For a full list of the instrumentation and a description of their performance, and for parameters generated by aircraft software, see the POST Web sites noted in section 1.

[12] Satellite remote sensing data are also archived on the POST Web site under the headings POST Field Catalog and Operational Products. It includes GOES, MODIS, QuikSCAT, and NexSat data and retrievals including upper air soundings. Satellite images and retrievals proved to be important in flight mission planning and subsequent data analysis.

2.2. Twin Otter Flights

[13] Each flight path of the 17 flights made by the TO originated from the airport in Marina, CA, located just north of Monterey on Monterey Bay. Except for flights TO4, TO9, and TO11, the TO proceeded WNW over the ocean to the vicinity of 123°10′W and 37°N, a distance of ~125 km from Marina. At that away point, the aircraft measurement of in-cloud wind velocity was used to start a horizontal quasi-Lagrangian zigzag pattern (termed QLP in the following; see Figure 2). The end of each line of the approximately E-W zigzag was ~20 km from the centerline of the pattern, and each E-W line had a horizontal slant in the windward direction depending on the air velocity in the Sc layer so that the average displacement of TO along the centerline matched the air velocity in the Sc. The nine daylight flights lasted from about 10:15 A.M. to 15:15 P.M. local time, and the eight nighttime flights lasted from about 18:00 P.M. to 23:00 P.M. local time. The flight duration of the QLP was ~3 h POST local time plus 7 h equals UTC time.

[14] A typical vertical flight pattern flown by TO during the zigzag is shown in Figure 3. Most of the vertical pattern consisted of "porpoising" through Sc top. The pilot of the TO was asked to ascend 100 m above cloud top and then descent 100 m below cloud top during porpoising at a vertical rate of ~1.5 m s^{-1} resulting in slant profiles with a sawtooth pattern. Figure 3 shows four sets of such patterns

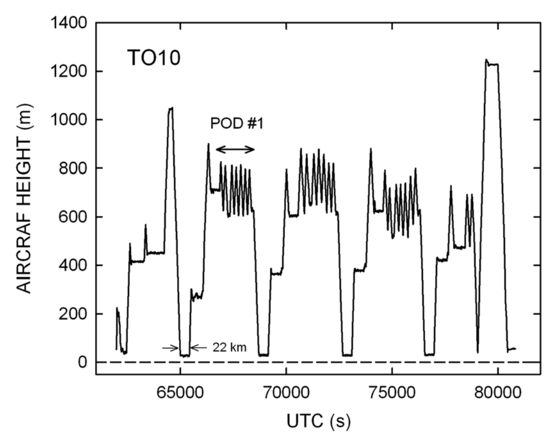

Figure 3. Vertical flight path of the Twin Otter aircraft during flight TO10. During the sawtooth patterns, given the name "pods," the aircraft flew slant paths profiles (porpoises) 100 m above and below cloud top. Horizontal legs ~22 km long were flown near the sea surface, just below cloud base, and within the cloud.

for TO10 which are given the name "pods" (for a detailed description of pods for POST flights as well as analyses of their EIL, see *Hill* [2012]). Similar vertical patterns have been used in Sc by *VanZanten and Duynkerke* [2002], for a brief time during DYCOMS II, and by *Katzwinkel et al.* [2011]. The rationale for using this pattern during POST was to observe in detail structures above and below Sc top involved in the entrainment process. A total of about 900 passes was made through Sc top during the POST flights. Between each pod, the aircraft descended to just above the sea surface for horizontal flight over a total of ~80 km to estimate surface fluxes. Similar horizontal flight sections were made for most flights just below cloud base and in-cloud. At least one higher sounding was made for each flight.

2.3. Average Flight Properties

[15] Table 1 lists POST flights, defines parameters measured on the TO, and lists parameter averages that relate to this study. Flights TO4 and TO11 are not included, because the former is made across the prevailing wind direction and the latter is flown in an area just filling with Sc. Some similar parameters from DYCOMS II Sc [*Gerber et al.*, 2005] are added to Table 1. All POST parameters in Table 1 are averages of measurements from ~10 TO profiles through cloud top spaced apart approximately equally in time, except for z_i, $z_i - z_o$, dz_i/dt. The z_i parameters are averages for all penetration through Sc top, and z_o are averages from cloud base penetrations that numbered about six for each flight. The parameters, except for the noted exceptions, do not take advantage of the larger number of ~50 profiles made above cloud top for each flight, thus the parameters in Table 1 do not have the most accurate averages possible. All height values are from the TO radar altimeter. (For another listing of POST parameters and plots, see *Wang* [2009]).

[16] Uncertainty exists in choosing the jump values listed in Table 1, which is consistent with earlier conclusions concerning the difficulty of choosing jumps above Sc [*Siems et al.*, 1990; *Shao et al.*, 1997; *Wang and Albrecht*, 1994; *Moeng et al.*, 2005]. The difficulty for POST Sc comes from two effects: The shallow slant angle of the TO during porpoising, resulting from the aircraft speed of ~50 m s^{-1} and an ascend/descend rate of ~1.5 m s^{-1}, causes the penetration of the top and bottom of the EIL to be separated horizontally ~1.5 km given a mean EIL thickness of $\Delta z = 45$ m. Jump estimates for individual ascends/descends are error prone because of the vertical variability of the Sc cloud top surface, so that jumps must rely on averages from multiple porpoises.

[17] The second effect relates to choosing the height of the bottom and top of the EIL. Choosing the bottom requires an assumption because the shallow slant angle of the TO occasionally causes penetrations of cloud segments above the unbroken Sc. Here we define the bottom of the EIL and cloud top z_i as the height above which LWC < 0.01 g m^{-3} and where cloud segments found more than 5 s above the solid cloud are ignored. Above z_i the EIL has different layers as described by *Moeng et al.* [2005], *Wang et al.* [2008], *Katzwinkel et al.* [2011], and *Malinowski et al.* [2013]. Here an approach similar to the one described by *Yamaguchi and Randall* [2012] is used for choosing EIL top by calculating dT/dz above z_i. Under ideal conditions, this produces a Gaussian-type curve from which the upper limit of the EIL is picked for the present study when dT/dz is ~10% of the curve's maximum. The ideal condition is not always observed for POST flights given the complexity and variability of the EIL caused by turbulence and unexpected layers situated above cloud top. In those cases, a combination of 1 Hz LWC, T, q_v, U, and $U_{\theta s}$ data from porpoising profiles is used to subjectively estimate the upper limit of the EIL

[18] Additional aspects of Table 1 include the following: (1) Mean wind direction measured by the TO at cloud top, $U_{\theta i} = 332°$, is nearly the same as the ~328° orientation of the CA Coast; however, 8 of 15 flights have a wind direction from the continent either in-cloud or above cloud. (2) All flights show vertical wind shear U_s near cloud top, with some flights showing large values. The shear is estimated by calculating the largest value of dU/dz and dividing by the layer thickness (Δz_s) over which it occurs. This layer is frequently found just above cloud top. Large uncertainties exist in the average shear values given the turbulent nature of the cloud top environment. (3) Values of dz_i/dt are calculated by using linear regression of the relationship between z_i and flight time for all cloud top penetrations. (4) TO3 shows $dz_i/dt \sim 0$ cm s^{-1}, TO10 shows the fastest lowering of cloud top, TO13 has the fastest rising of cloud top and the smallest temperature jump ΔT, and night flight TO6 has an extensive higher cloud cover and rapidly lowering cloud top.

3. Entrainment Measurements

3.1. Method

[19] The mixed layer theory of *Lilly* [1968] predicts that w_e can be determined using the "flux-jump" approach given by

$$w_e \;=\; < w \times \phi > / \, \Delta\phi \tag{1}$$

where ϕ is a conserved scalar quantity that has a large difference between the top of the cloud and the free atmosphere above the EIL, $<w \times \phi>$ is the vertical flux of the entrained conserved scalar at cloud top, w is the vertical velocity, and $\Delta\phi$ is the scalar's jump across the EIL. Angled brackets indicate averages.

[20] A variation of the flux-jump approach for estimating w_e is applied to the POST Sc by using conditional sampling to identify parcels (cloud holes) that contain the conserved scalar entrained into the Sc. This approach has been applied previously by *Nicholls* [1989], *Khalsa* [1993], *Wang and Albrecht* [1994], *Wang and Lenschow* [1995], and *Gerber* [1996] using scalars including ozone, dimethyl sulfide, and q_t.

[21] The q_t scalar is again used for the POST Sc to estimate w_e such as done by *Gerber et al.* [2005]:

$$w_e = A_r < w'\left[\left(LWC'/\rho\right) + q_v'\right] > / \, \Delta q_t = F_e / \, \Delta qt \tag{2}$$

where the primed parameters represent differences between the value of the parameters in the hole and the value adjacent to the hole unaffected by entrainment, A_r is the sum of all horizontal dimension of the holes divided by the total flight distance, q_v is the water vapor mixing ratio, ρ is air density, and Δq_t is the jump across the EIL ($\Delta q_t = \mathrm{LWC}_i/\rho + \Delta q_v$). F_e is defined as the entrainment mass flux with units g kg^{-1} m s^{-1} where g is the mass of the scalar in a kilogram of atmospheric air, and m s^{-1} are units for w.

[22] LWC measured by the PVM is called the "indicator variable" [*Khalsa*, 1993] used to identify the location and

Table 1. Average Properties Calculated From 10 Vertical Profiles for Each POST Flight[a]

Flight		Date (UTC)	z_i (m)	$z_i - z_o$ (m)	Δz (m)	dz_i/dt (cm/s)	T_i (°C)	ΔT (°C)	LWC_i (g/m^3)	q_{vi} (g/kg)	Δq_v (g/kg)	U_i (m/s)	U_s (1/s)	$U_{\theta i}$ (deg)	$U_{\theta s}$ (deg)
TO1[b]	D	7/16	560	365	34	−0.17	10.6	5.9	0.48	8.66	+2.02	8.40	0.056	336	+22
TO2[b]	D	7/17	529	219	32	−0.49	9.8	7.4	0.33	7.99	−2.72	11.0	0.119	336	−23
TO3[b]	N	7/19	500	264	52	+0.35	10.3	10.1	0.46	8.29	−3.65	14.5	0.183	333	+14
TO5[bc]	N	7/28	486	253	41	+0.76	10.8	2.8	0.30	8.70	−0.71	11.6	0.352	335	+2
TO6[b]	N	7/29	638	275	20	−1.32	9.4	7.5	0.50	7.88	−5.94	9.50	0.151	331	−1
TO7	D	7/30	375	282	50	+0.01	12.7	2.9	0.33	9.06	−0.27	13.2	0.108	330	+9
TO8[bc]	D	8/1	413	82	43	−0.68	12.8	3.5	0.22	9.73	−0.83	17.4	0.133	340	+8
TO9[d]	D	8/2	182	127	57	+0.08	11.4	8.3	0.21	8.61	−0.88	12.7	0.092	324	+5
TO10	D	8/4	635	269	34	−2.30	9.7	8.7	0.39	8.04	−5.70	9.9	0.183	331	+3
TO12	N	8/8	760	329	29	−0.62	9.0	8.9	0.50	7.81	−4.67	6.5	0.235	320	−24
TO13[c]	N	8/9	654	409	59	+0.93	10.4	2.3	0.29	8.50	−0.49	10.9	0.190	328	+2
TO14	N	8/12	545	416	31	−0.08	11.7	6.4	0.59	9.22	−1.47	13.9	0.069	333	+6
TO15	N	8/13	495	314	62	+0.79	10.5	9.5	0.03	9.00	−1.30	14.6	0.141	341	+13
TO16[e]	D	8/14	457	326	70	+0.38	11.5	10.2	0.42	9.00	−3.04	7.6	0.099	325	+5
TO17	D	8/15	454	329	59	+0.08	11.8	6.8	0.47	9.12	+0.21	9.3	0.093	330	−7
POST Mean			513	284	45		10.8	6.7	0.39	8.64	−1.96	11.4	0.145	332	+2
DYCOMS II Mean			756	360	23		11.6	8.2	0.67	9.36	−5.93				

[a]z_i, height of cloud top; z_o, height of cloud base; Δz, height change across the entrainment interface layer (EIL); dz_i/dt, rate of change of cloud top; T_i, temperature at cloud top; ΔT, temperature jump across EIL; LWC_i, liquid water content at cloud top; q_{vi}, vapor mixing ratio at cloud top; Δq_v, jump of vapor mixing ratio across EIL; U_i, wind speed at cloud top; U_s, wind shear above cloud top; $U_{\theta i}$, wind direction at cloud top; $U_{\theta s}$, change in wind direction between z_i and the top of the EIL; D, day flight; N, night flight.

[b]Some deviation from Lagrangian flight pattern.

[c]Uncertainty in Δ jumps.

[d]Not Lagrangian, N-S flight along coast.

[e]No UFT data.

horizontal dimension of entrained parcels (cloud holes) and to calculate *LWC′*. All POST flights show holes with reduced LWC, and the holes are readily identifiable. Figure 4 gives an example of holes identified during one porpoise below Sc top on flight TO10. The assumption is made that the narrow regions of reduced LWC (blue) are due to evaporation or dilution of cloud water caused by entrainment. The criterion used for identifying holes also requires that LWC > 0.01 g m^{-3}. Breaks in otherwise solid Sc rarely occurred in QLP portions of the POST flights. The Sc occasionally showed LWC = 0 g m^{-3}, with TO9 having the greatest percentage 0.6% of holes without LWC along the flight track, and with all other flights having percentages <0.5%.

[23] Equation (2) also requires values for q_v' within the LWC holes. Given the slow rate of q_v data measured on the TO, 50 Hz UFT in-cloud temperature data is used instead to estimate q_v by assuming that holes with reduced LWC are at water saturation where q_s (saturation water vapor mixing ratio) is calculated with the Clausius-Clapeyron relationship. Support for this assumption comes from earlier tethered-balloon observations in FIRE Sc [*Albrecht et al.*, 1988] with the saturation hygrometer [*Gerber*, 1980], from a slant profile in Sc with the hygrometer on a motorized airship [*Gerber*, 1994], and from the hygrometer measurements [*Gerber*, 1991] in turbulent and unbroken radiation fog with a large vertical temperature gradient. In all three cases measured relative humidity (RH) only varied between 99.5% and 100.5%. The differences between q_v and q_s for this RH range are small.

[24] The method for picking out holes from the LWC data is detailed in *Gerber et al*. [2005], and the same procedure is used here. A brief description of the procedure follows: A running average of LWC data over 400 m of flight path is used to establish average LWC background values. The average values are multiplied by a constant K1 = 0.97 and all LWC data in the 50 Hz record are deleted if they are smaller than this average. The resulting gaps in the 50 Hz data are closed by extrapolation, and the 50 Hz data is again given a new running average over 400 m which is multiplied by K2 = 0.94. The original 50 Hz LWC data is then compared to the new LWC average and all original 50 Hz data with LWC less than the new LWC average are identified as LWC holes created by entrainment. A similar procedure is used for UFT-M data (K3 = 0.998) to find deviations from average background *T* data after trend removal to calculate values of q_v' within holes. The use of the K constants reduces the effect of small amplitude noise in the 50 Hz data. The values of *w* used in equation (2) are referenced to a 3 km running mean of the 50 Hz *w* data, which removes most of the residual vertical velocities due to the aircraft porpoising and gives $\langle w \rangle = 0$ m s^{-1}.

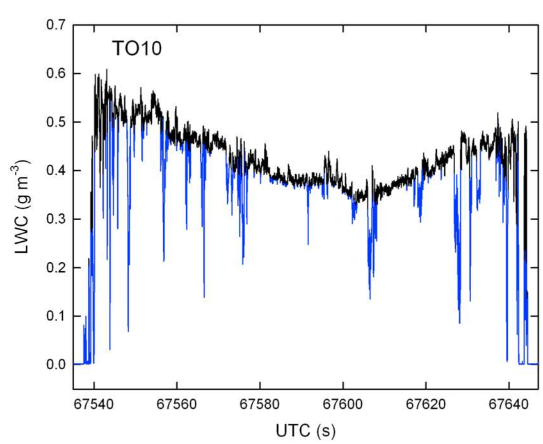

Figure 4. One porpoise down and up through ~100 m of the Sc on flight TO10 showing 50 Hz LWC (black line) as a function of flight time. Cloud holes with narrow regions of reduced LWC (blue lines) are chosen by conditional sampling and are assumed to form by the entrainment process.

Table 2. Average Entrainment Velocity (w_e) and Entrainment Flux (F_e) Calculated Using 10 Profiles Above Cloud Top for Each POST Flight[a]

Flight No.	w_e (mm/s)	$\sigma(w_e)$ (mm/s)	F_e (g/kg m/s)	$\sigma(F_e)$ (g/kg m/s)
TO1	5.3	4.0	0.0082	0.0053
TO2	1.5	0.4	0.0045	0.0008
TO3	7.5	2.7	0.0310	0.0032
TO5	12.4	12.8	0.0126	0.0024
TO6	2.1	0.6	0.0135	0.0022
TO7	18.2	9.8	0.0110	0.0018
TO8	3.8	33.2	0.0040	0.0013
TO9	4.3	4.3	0.0047	0.0007
TO10	1.4	0.3	0.0084	0.0016
TO12	2.5	0.7	0.0130	0.0037
TO13	27.2	134.4	0.0224	0.0045
TO14	9.2	1.8	0.0190	0.0030
TO15	11.0	5.6	0.0172	0.0033
TO16	2.4	0.5	0.0083	0.0003
TO17	2.5	3.2	0.0078	0.0008

[a]One standard deviation of the uncertainty of each parameter is given by σ.

3.2. Entrainment Flux and Velocity

[25] A surprising observation in POST Sc is the sign of the LWC′ flux (LWC′ × w') in conditionally sampled holes. The expected sign is positive which corresponds to the product of negative values for LWC′ and for w' of descending holes, such as found for one flight during DYCOMS II [see *Gerber et al.*, 2005, Figure 4]. Instead for some POST Sc, LWC′ flux shows negative values indicating that $w > 0$ m s^{-1} and that the holes are ascending. This effect is strongest near Sc top. The expected q_v' flux should also be positive near cloud top given the smaller value of q_v in cooled and descending holes in comparison to q_v in the adjacent cloud unaffected by entrainment. However, some negative values of q_v' flux are also found in the Sc. This means that q_v' must be positive and corresponds to descending holes that are warmer than the adjacent cloud. A final possibility is that warmer holes ascend. The warmer holes suggest that water droplets are evaporating in those holes. All flights show a significant number of warm holes except for (classical) flights TO6, TO9, TO10, TO12, TO16, and TO17 that show behavior similar to Figure 4 in *Gerber et al.* [2005]. This surprising behavior of the entrainment fluxes in the other POST Sc ("non-classical" flights) is likely a result of strong mixing near cloud top due to wind shear that also increases the uncertainty of applying equation (2).

[26] The procedure for finding the average influence of cloud holes on F_e for each POST flight consists of first translating vertically all porpoising data so that the height of all cloud tops is identical. Second, it is necessary to establish an approach that deals with the observed ascending and descending holes in estimation F_e. The observations show that the average F_e is often smaller close to cloud top than deeper in the cloud and that the average has an approximate value of zero close to cloud top for Sc with strong shear and mixing at the cloud top interface. Given the abundance of observed holes in the Sc, especially near cloud top, the estimation of w_e using such average values of F_e at cloud top for equation (2) obviously leads to unrealistic results. The approach used here instead hypothesizes that some observed holes just below cloud top are lost by crossing the turbulent and mixing cloud top interface (detrain) and lose all LWC by evaporation thus moistening the EIL. The assumption is made that detraining holes are identified by holes that are ascending just below cloud top. Applying this assumption to equation (2), except for warm descending holes, is consistent with giving all other ascending fluxes positive values in equation (2) which produces more realistic values of F_e at cloud top needed to estimate w_e, especially for the non-classical Sc. The w_e estimated in this fashion then represents the reduction of LWC both by the entrainment of drier air and by the evaporation of LWC at cloud top.

[27] The 50 Hz LWC, UFT-M, and gust probe data, and the jumps listed in Table 1 are used to calculate F_e and w_e for all flights given the above approach. F_e is averaged over 10 m increments below cloud top, and linear regression is used to extrapolate the F_e versus height relationship to cloud top where F_e is divided by Δq_t to produce w_e. Table 2 lists values of F_e and w_e resulting from this procedure.

[28] Figure 5 shows w_e for all flights listed in Table 2 as a function of vertical wind shear U_s. Several trends are apparent in Figure 5. Daytime w_e values are significantly smaller than nighttime w_e values as has been noted previously [e.g., see *Gerber et al.*, 2005]. The largest values of w_e correspond to the weakest static stability of the EIL as indicated by the smallest ΔT values listed in Table 1 for flights TO5, TO7, and TO13. Both daytime and nighttime w_e values show a tendency of decreasing w_e with increasing wind shear, although the scatter and limited number of data points in Figure 5 prevent a firm conclusion. The trend is not followed by TO5 which has a large w_e that may be related to the small ΔT jump for TO5. Decreasing w_e with increasing wind shear agrees with the finding by *Katzwinkel et al.* [2011], but disagrees with the large eddy simulation (LES) of a Sc with strong wind shear [*Wang et al.*, 2012].

[29] The w_e values shown in Figure 5 and Table 2 can be compared to some recently published w_e values for Sc found in *Faloona et al.* [2005], *Gerber et al.* [2005], *Wang et al.* [2008, 2012], *Caldwell and Bretherton* [2009], and *Katzwinkel et al.* [2011]. Most values of w_e are within an order of magnitude, but some differences are found. The Gerber et al. values are about 2 times larger than those from

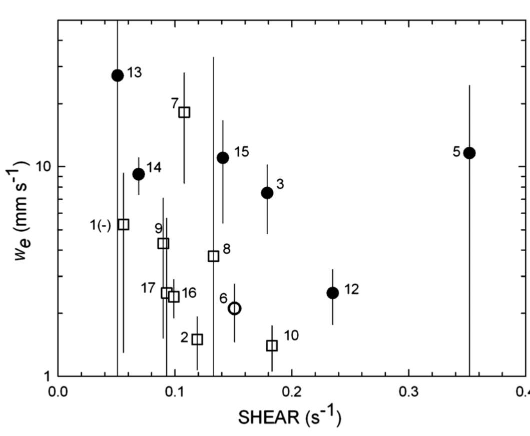

Figure 5. Entrainment velocity w_e as a function of vertical wind shear near Sc top for POST flights (numbered). Open squares indicate daytime flights, solid circles are nighttime flights, and the open circle is a nighttime flight with a high overcast. Vertical lines are ±1 standard deviation of the w_e measurement variability.

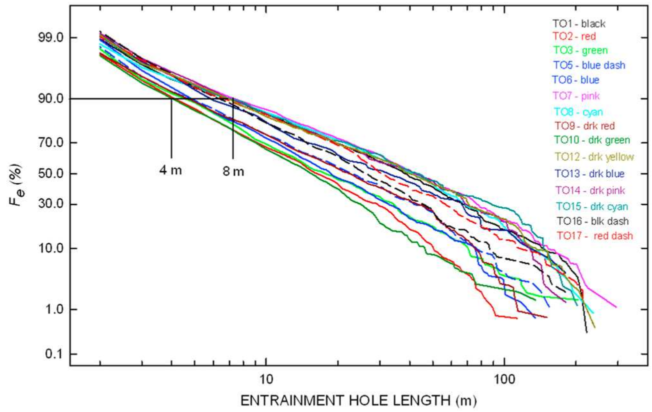

Figure 6. Log probability of the entrainment mass flux F_e as a function of entrainment hole length measured during aircraft porpoising through Sc on POST flights. The 4 m and 8 m numbers indicate the minimum lengths that must be measured to achieve 90% of F_e.

Falloona et al., with both sets of w_e measured on the same aircraft during DYCOMS II. Values given by Wang et al. and Katzwinkel et al. are for the top of the EIL rather than at cloud top making for a questionable comparison. The LES-predicted average diurnal values from Caldwell and Bretherton are close to average values estimated for POST, but the LES modeling required some "tuning" to provide reasonable values.

[30] It is also of interest to compare the w_e values in Table 2 to calculations for POST Sc by *Carman et al*. [2012] of TKE (turbulent kinetic energy) assumed to be consumed by the entrainment process. The data in their Figure 8 have nine TKE values that can be compared to nine w_e values in corresponding POST flights. The square of the correlation coefficient (R^2) between the two parameters is 0.207. This small value of R^2 is caused by values of TKE and w_e for flight TO3 which has the strongest directional wind shear at cloud top. Excluding TO3 from the correlation results in $R^2 = 0.858$.

[31] The measurement of F_e in all holes and their horizontal lengths makes it possible to construct log probability plots of F_e versus hole length as shown in Figure 6. The relationship between F_e and length is approximately lognormal for all flights but shows significant difference between flights. F_e lengths vary about a factor of 2 for small lengths and a factor of 4 for lengths of ~100 m. The contribution to F_e for lengths of >100 m falls off faster than the lognormal behavior. The 4 m and 8 m lengths indicated in Figure 6 show horizontal lengths that measurements and models need to resolve to capture 90% of F_e in such Sc. The curves in Figure 6 also have bearing on conceptual ideas of how Sc entrain. For example, the small-scale entrainment on Sc cloud top domes and "engulfment" at downwelling areas shown in the conceptual sketch of Sc by *Wood* [2012] appear to be inconsistent with the continuous curves in Figure 6.

3.3. Analysis of Flights TO3, TO10, and TO13

[32] Flights TO3, TO10, and TO13 are chosen and analyzed in greater detail (see *Malinowski et al*. [2013] for additional descriptions of TO10 and TO13). These three flights illustrate the wide-ranging behavior of the POST Sc, and they give new insight in how entrainment in such Sc should be viewed. Rather than evaluating 10 vertical profiles during porpoising as done in the preceding, all ~50 profiles are evaluated for each flight. Some of the parameters shown in Table 1 are recalculated in Table 3 using all profiles. Comparison of Table 2 with Table 3 parameters shows that the 10 profiles used for the former are in reasonable agreement with the 50-profile results.

[33] Figures 7 and 8 compare the three flights to illustrate their large differences for dz_i/dt and F_e. Figure 7 shows the rate of change of cloud top and of the top of the EIL as a function of flight time during QLP of each flight. The dashed lines in Figure 7 are constructed using linear regression of the data and provide the average change of cloud height and of the EIL. The regression line for night flight TO3 ends at ~15,000 s UTC, because the remainder of the flight is outside of QLP. In the plot for daytime flight TO10, the regression line is applied only to data for UTC > 70,000 s when cloud top rapidly decreases. Nighttime flight TO13 is unique, because cloud top grows rapidly through an adjacent layer with nearly the same q_v as the average q_v in the cloud, and with the smallest value of ΔT of any flight.

[34] The behavior of F_e as a function of height below cloud top is shown in Figure 8. The data points represent averages of F_e over 10 m increments below cloud top. Linear regression is used to generate the dashed lines that extrapolate data to cloud top to produce F_e values used to calculate w_e with equation (2). F_e for TO10 is much smaller than for the two night flights as expected. Two dashed lines are applied to F_e for TO3. One is applied to the approximately linear behavior of F_e for $zi - z > {\sim}20$ m, and the second takes into account the unexpected sharp increase in the F_e data near cloud top. Thus, the usual assumption of the linear dependence of

Table 3. Average Parameter Values Recalculated Using All Profiles (~50) Made During Each of the Three POST Flights[a]

Flight No.	Δz (m)	LWC$_i$ (g/m^3)	q_{vi} (g/kg)	Δq_v (g/kg)	T_i (°C)	ΔT (°C)	U_i (m/s)	ΔU (m/s)	U_s (1/s)	Δz_s (m)	w_e (mm/s)
TO3 A	43.5	0.41	7.98	−2.91	10.5	9.9	15.0	1.4	0.295	11.7	9.3
	11.9	0.07	0.50	−0.83	0.5	1.0	1.2	1.3	0.252	6.9	2.7
TO3 B	32.2	0.42	8.05	−2.08	10.4	9.3	14.5	1.5	0.314	-	-
	14.6	0.09	0.54	−0.83	0.3	0.8	0.6	0.6	0.226	-	-
TO10	32.8	0.41	7.98	−6.17	10.0	9.5	9.6	−4.8	0.211	28.6	1.3
	13.0	0.10	0.11	−0.17	0.3	0.5	1.0	−1.2	0.110	14.9	0.2
TO13 A	59.8	0.32	8.50	−0.51	10.4	2.6	10.4	1.5	0.167	16.2	24.6
	38.1	0.19	0.25	−1.1	0.4	1.6	1.2	1.1	0.138	12.4	42.0
TO13 B	-	0.28	-	+0.11	-	2.1	-	-	-	-	133.3
	-	0.16	-	+0.20	-	1.0	-	-	-	-	1033.4

[a]The parameters are defined in Table 1 except for Δz_s which is the layer thickness near cloud top over which U_s is estimated. The quantities in the line following each flight number are parameter averages. The line below each flight number contains the parameters' one standard deviation.

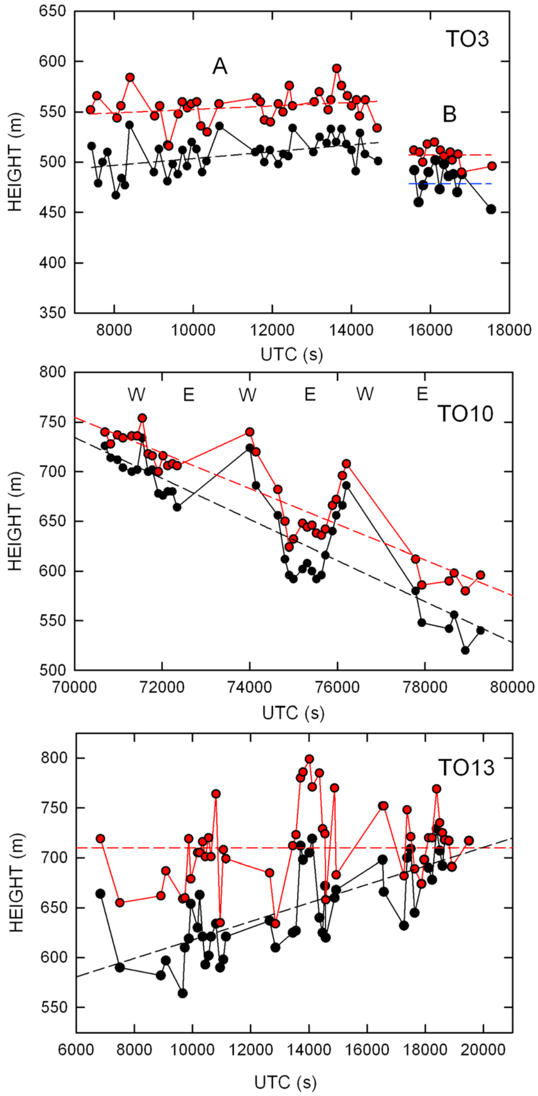

Figure 7. The height of cloud top (black circles and lines) and the height of the top of the EIL (red circles and lines) as a function of time during the quasi-Lagrangian flight times for flights TO3, TO10, and TO13. A and B are two different sections of flight TO3. W and E indicate the times for TO10 when the aircraft was farthest east and west during the zigzag flight pattern. Dashed lines are least squares fit to data.

entrainment flux with height below cloud top does not always hold and can lead to significant differences of F_e at cloud top. Other flights showing sharp increases of F_e near cloud top are TO1, TO16, and TO17. The interpretation of these increases is that they relate to detrainment at cloud top. (See http://www.gerberscience.com/POSTdata/POSTdata.html, for plots of F_e versus height below cloud top for other POST flights).

3.3.1. Flight TO3

[35] TO3 differs in several aspects from the other two flights. Most obvious is the clearing of Sc observed NNW of the flight track as shown in Figure 1. Satellite imagery shows the clearing advancing SSE faster than the progression of the TO during the QLP for this flight. TO3 also differs in that its QLP required modification (after ~15,000 UTC), because the TO was approaching restricted airspace. Figure 9 shows the actual TO3 QLP with the primary pattern labeled A and the modified pattern labeled B which is located ~40 km E of the centerline of pattern A. Table 3 lists parameter values for the two patterns. Figure 7 shows that the EIL is significantly thinner for B and that cloud top is ~40 m lower for B. The latter indicates that cloud top for TO3 is tilted upward E to W which causes baroclinic behavior that is a common feature associated with Sc off the California coast [*Brost et al.*, 1982a].

[36] Figure 10 shows measurements from a typical vertical profile from pattern A. Horizontal lines bracket the EIL chosen from large changes in the vertical gradients of T, U, and U_θ. The measurements show vertical wind shear and clockwise rotation of wind in the EIL and show that U has a peak in the EIL that can be a result of thermal wind caused by certain sea surface temperature gradients [*Gerber et al.*, 1989]. The wind above the EIL is dry and of continental origin. The strongest wind shear gradient and its location close to cloud top are similar to the strong wind shear case modeled

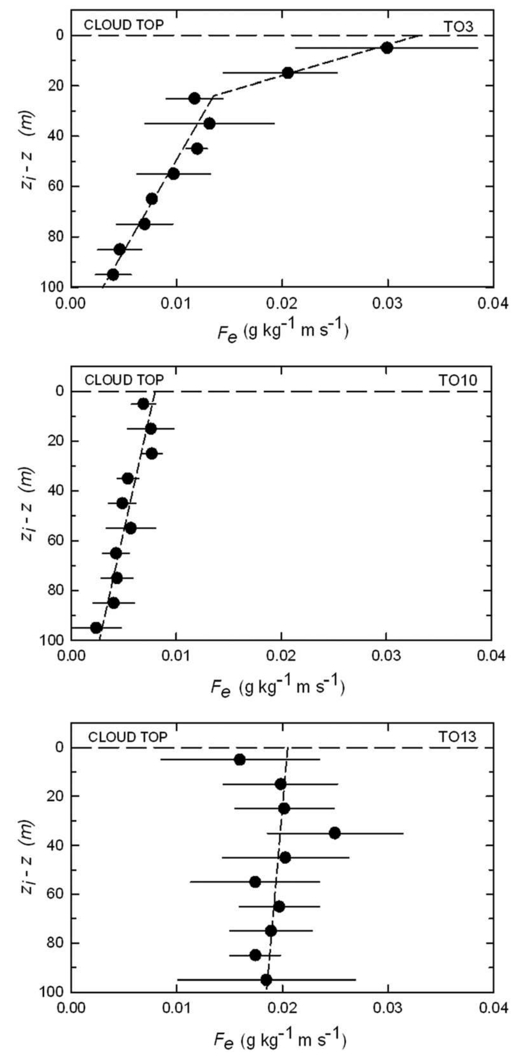

Figure 8. Average values of the entrainment mass flux F_e as a function of height below cloud top ($z_i - z$) for flights TO3, TO10, and TO13. Horizontal lines are ±1 standard deviation of the F_e measurements. Dashed lines are linear regression fits to the data.

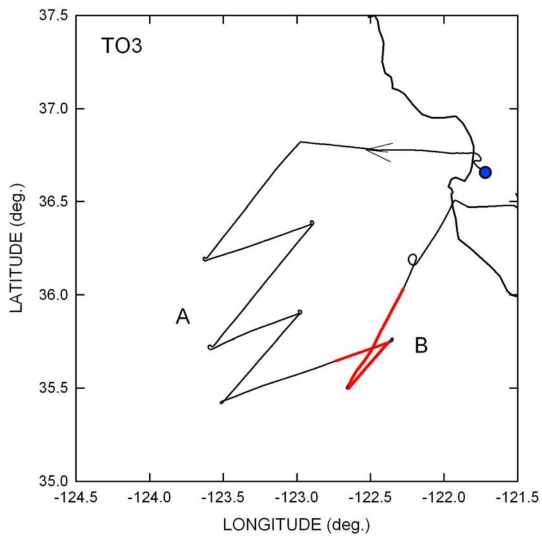

Figure 9. Flight path of the aircraft during flight TO3. A (black) is next to the intended quasi-Lagrangian zigzag pattern, and B (red) is a deviation from the pattern caused by restricted airspace. B is closer to the continent and has different Sc properties than Sc for A (see text and Table 3).

by *Wang et al.* [2012] for a VOCALS Sc near the South American continent.

[37] The strong directional wind shear at cloud top causes mixing through a deep layer of the Sc as illustrated in the left plot of Figure 11 where the contributions of LWC′ and q_v' fluxes to F_e are given without being assigned positive values. The large number of F_e values on either side of $F_e = 0$ in the left plot indicates the presence of strong mixing with the strongest mixing within ~20 m below cloud top, which is also reflected in the increase of F_e near cloud top shown in Figure 8. The data in the right plot show only q_v' values in descending cloud holes with temperature warmer than the adjacent unaffected cloud. Thus, warm air from above cloud top entrains into the Sc and is apparently evaporating cloud water deep in the cloud. This process must be related to the rapid dissipation of the Sc upwind of the QLP. *de Roode and Wang* [2007] have suggested that strong wind shear could dissipate Sc.

3.3.2. Flight TO10

[38] The lowering of cloud top height as a function of time ($dz_i/dt \sim 23\,\mathrm{mm\,s^{-1}}$) during the TO10 QLP is fastest compared to this change for all other POST flights. The change for TO10 far exceeds $w_e = 1.3\,\mathrm{mm\,s^{-1}}$ calculated using equation (2) for this flight. At first glance, this suggests that the flux-jump equations appear inadequate for calculating entrainment for TO10.

[39] The entrainment velocity w_e can be estimated in another way for TO10 using the "difference method" [*Stevens et al.*, 2003b] given by

$$w_e = \frac{dz_i}{dt} - Dz_i \tag{3}$$

where D is the large scale divergence and and Dz_i is the mean subsidence velocity (U_{sub}). *Faloona et al.* [2005] gives U_{sub} in Sc off the California coast during DYCOMS II as ~2 mm s^{-1}, and *Wood and Bretherton* [2004] give U_{sub} an average range of 2–4 mm s^{-1}. Inserting these estimates of U_{sub} into equation (4) yields an unrealistic value of $w_e \sim 20\,\mathrm{mm\,s^{-1}}$ for TO10. Figure 7 shows that the height of the EIL top during the TO10 QLP also rapidly decreases. This suggests that subsidence for TO10 was much larger than the given U_{sub} averages, possibly caused by advection of continental air above cloud top which is consistent with the shift in the wind direction in the EIL. Dry air flowing off the California continent, sometimes termed the "Santa Ana" wind, can rapidly lower the boundary layer [*Gerber*, 1986; see also *Sundararajan and Tjernstrom*, 2000]. Other possibilities include the location of the QLP for TO10 in an exceptionally strong descending branch of a sea breeze circulation, and the location of the QLP in a gradient in the slope of the inversion as suggested by the changing difference in the heights of the E-W zigzag as shown in Figure 7. These phenomena are possible explanations for the rapidly lowering TO10 boundary layer rather than assigning the lowering to w_e.

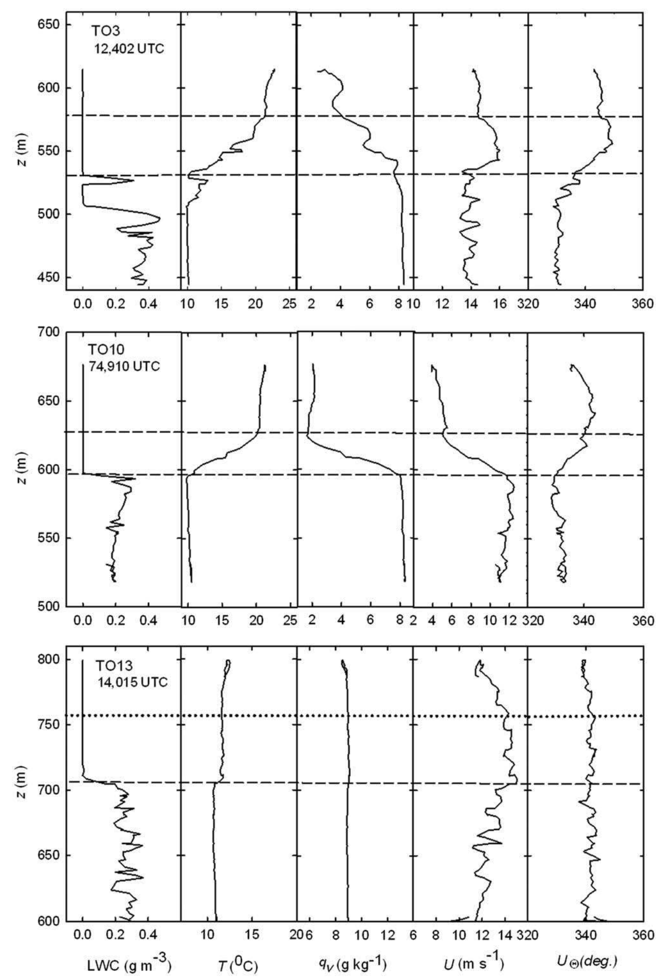

Figure 10. One typical vertical slant profile from flight TO3, TO10, and TO13 of LWC (liquid water content), T (air temperature), q_v (water vapor mixing ratio), U (wind speed), and U_Θ (wind direction) as a function of z (height above ocean surface). Dashed lines show bottom and top of the EIL (Entrainment Interface Layer), except for flight TO13 where the dotted line is the distance above cloud top corresponding to the mean thickness of the moist layer adjacent to cloud top.

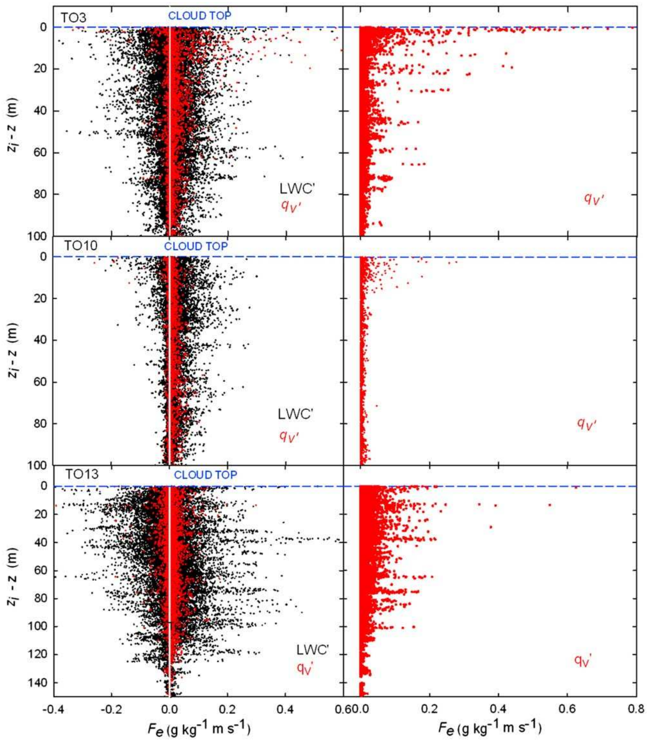

Figure 11. Fifty hertz data points for F_e (all measured positive and negative values are shown) as a function of height below cloud top ($z_i - z$) for flights TO3, TO10, and TO13. Left plots give the contribution to F_e from holes with depleted LWC′ (black data) and with q_v' (red data). Right plots show only q_v' data corresponding to descending holes with temperature warmer than adjacent cloud unaffected by entrainment.

[40] Figure 11 shows vertical profiles of F_e for TO10. The left plot in Figure 11 shows that most of the F_e values fall to the right of the $F_e = 0$ which is expected if entrainment is of classical nature where cooled entrained parcels sink and the flux-jump expressions hold. This conclusion is also supported by the linear dependence of the average F_e with height for TO10 as shown in Figure 8. Some negative LWC′ values are seen close to cloud top in Figure 11 indicating some mixing. The right plot in Figure 11 shows nearly constant small values of q_v' with height suggesting that a minimal amount of warm air from the EIL is entrained. TO10 cloud top is lowering faster than the EIL shown by the ~25 m difference between both levels during the QLP in Figure 7. This suggests that the Sc are dissipating due to evaporation at cloud top. Toward the end of the QLP for TO10, a moist layer developed just above cloud top supporting this suggestion.

[41] Figure 10 shows measurements from a typical vertical profile for TO10. Again, the top of the EIL is chosen by noting large changes in the vertical gradients of the parameters. The TO10 profile is similar to the profile for TO3 in that U also has a clockwise rotation in the EIL. Differences include a large reduction in U between the cloud and above the EIL and a different shape of the average vertical gradient of wind shear and the other parameters in the EIL. The shapes are approximately linear in the EIL for TO10 as also found in the Sc study by *Katzwinkel et al*. [2011]. However, the wind shear gradients in TO10 differ in that ~1/3 of the gradients in the rest of the profiles are much steeper and resemble the large wind shear gradients found near cloud top for TO3. The average value for Δz_s shown in Table 3 is not much different from the average value of EIL thickness Δz; but when only one third of the profiles with steeper gradients are considered, then $\Delta z_s \sim 0.35\ \Delta z$. This behavior is similar to that described by *Kurowski et al*. [2009] where large convective eddies in the Sc are suggested to "squeeze" the EIL thus enhancing the local shear and reducing the gradient Richardson number. This effect is observed for TO10 profiles as shown in Figure 12 where an approximate dependence is seen between the decreasing thickness of the EIL and increasing wind shear, an effect also shown by *Katzwinkel et al*. [2011]. The wind shear profiles in TO10 as well as in the *Katzwinkel et al*. [2011] Sc case may be unusual, because sharp vertical gradients of wind shear in the rest of the POST flights are usually found just above cloud top, as also noted by *Carman et al*. [2012] for POST Sc.

3.3.3. Flight TO13

[42] Flight TO13 is a unique POST flight because its QLP shows the most rapid increase in the height of cloud top (~10 mm s^{-1}) that grows primarily through a moist preexisting layer with the smallest ΔT and Δq_v of any flight. In Table 3, two sets of parameter averages are labeled A and B for TO13. The A averages correspond to all vertical profiles from the entire QLP shown in Figure 7, while B averages omit about 10% of the vertical profiles where jumps between cloud top and the atmosphere above the EIL are evident. The B averages are for profiles where the cloud grows into the moist layer where an upper limit of the EIL could not be identified. Table 3 also shows that the average value Δq_v in B is slightly positive indicating a larger q_v in the moist layer than in the cloud.

[43] Both the small values of ΔT and Δq_v adjacent to cloud top and the wind shear above cloud top must have contributed to the large values of w_e shown in Table 3 for A and B. The large w_e values are unrealistic given that both values are significantly larger than the rate at which cloud top rises. Small values ΔT and Δq_v and wind shear must also have influenced the strong mixing within the cloud as illustrated in Figure 11. The left plot shows large positive and negative

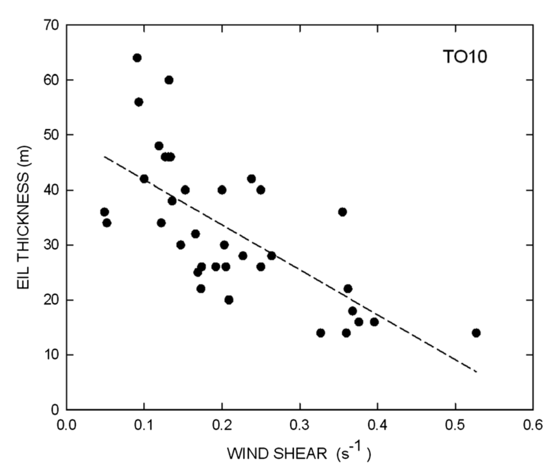

Figure 12. Vertical wind shear near Sc top as a function of EIL thickness for flight TO10 suggesting an inverse relationship (see text).

Table 4. Average Predicted Values of b^*, χ^*, and δT_p From Mixture Fraction Analysis, and Measured Average Temperature Change δT_m in Cloud Holes[a]

Flight No.	b^* (m s^{-2})	χ^*	δT_p (°C)	δT_m (°C)
1	0.0962	0.549	2.815	−0.040
2	0.0024	0.092	0.069	−0.056
3	0.0048	0.090	0.140	−0.091
5	0.0161	0.099	0.470	−0.034
6	−0.0059	0.086	−0.172	−0.096
7	0.0171	0.139	0.495	−0.026
8	0.0046	0.138	0.134	−0.011
9	0.0086	0.075	0.250	-
10	−0.0033	0.069	−0.097	−0.056
12	−0.0001	0.093	−0.003	−0.115
13	0.0175	0.360	0.506	−0.046
14	0.0123	0.190	0.358	−0.040
15	0.0106	0.088	0.310	−0.013
16	0.0061	0.089	0.194	-
17	0.0285	0.223	0.833	−0.029

[a]Buoyancy of the mixture at the boundary between cloudy and clear air is b^*, and the mixture fraction at this boundary is χ^*.

F_e fluxes of LWC′ and q_v' extending deep into the cloud indicating strong mixing. The right plot shows relatively large values of q_v' in warm descending holes decreasing approximately linearly downward, an observation also described for TO13 by *Malinowski et al*. [2010, 2011].

[44] Figure 10 shows measurements from a typical vertical profile from TO13. The dotted line in this plot differs from the upper limit of the EIL shown for TO3 and TO10 in that the dotted line in TO13 does not represent the top of the EIL but represents the mean distance between cloud top and top of the moist layer that remained at about the same level during the QLP. The minimal vertical changes of T and q_v between cloud top and the EIL are evident in Figure 10, and strong fluctuation in U are found high above cloud top. Figure 10 also shows that the directional wind shear U_Θ is minimal. The directional shear continues to be minimal as indicated by higher soundings for TO13. This suggests that the moist layer may have formed earlier by evaporation of other Sc, perhaps during the previous daylight period, and that the moist layer persisted for TO13 because of the minimal directional wind shear.

4. Microphysics

[45] The cooling of entrained air by LWC evaporation and by IR flux divergence near cloud top is key processes thought to affect the negative buoyancy that drives the circulation in Sc. It has been unclear to what degree each of the cooling effects plays. The Twin Otter data permit new insight on this uncertainty since it is possible with the 50 Hz temperature (UFT-M) and LWC (PVM) data to look at individual holes and to infer the importance of each cooling effect on the entrainment process. This look is limited to several POST flights chosen from prediction of the Sc "buoyancy reversal" effect as calculated from CTEI (cloud top entrainment instability) and from "mixture fraction analysis."

4.1. CTEI

[46] According to *Lilly* [1968], *Randall* [1980], and *Deardorff* [1980], the Sc layer can experience CTEI becoming unstable and dissipating given temperature and moisture jumps over the EIL that exceed certain values. The criterion for onset of instability is predicted to be caused by generation of negative buoyancy from cooling by LWC evaporation at cloud top under the condition that a parameter k exceeds a value of 0.23.

[47] An expression for k is given by *Kuo and Schubert* [1988]:

$$k = c_p \quad \Delta\theta_e/L \quad \Delta q \tag{4}$$

where c_p is the specific heat at constant pressure, $\Delta\theta_e$ is the jump in equivalent potential temperature, and L is the latent heat of vaporization.

[48] Another expression for k is given by *Stevens et al*. [2003b] as

$$k = 1 + \ \Delta s_l \ / \ L \quad \Delta q_t \tag{5}$$

where Δs_l is the jump in liquid water static energy.

[49] Observations in a number of studies [*Hanson*, 1984; *Albrecht et al*., 1985; *Nicholls and Turton*, 1986; *Kuo and Schubert*, 1988; *Gerber et al*., 2005] of Sc with $k > 0.23$ show that instability and breakup do not happen for those Sc. *MacVean and Mason* [1990] suggest instability onset values closer to $k = 0.7$ for Sc with mixing. Additional stability criteria are described by *Siems et al*. [1990] and *Duynkerke* [1993].

[50] Equations (4) and (5) are applied to jumps listed in Table 1 for POST flights and give nearly identical values of k. Only three flights are found with $k > 0.23$: $k = 0.451$ for TO6; $k = 0.354$ for TO10; and $k = 0.377$ for TO12. While these k values indicate that direct mixing between cloud top and free atmosphere causes buoyancy reversal, Sc again show no tendency for dissipation and breakup during the QLP flight periods.

4.2. Mixture Fraction Analysis

[51] Mixture fraction analysis relates buoyancy (b) of mixtures consisting of cloudy air at cloud top and of air above the EIL to mixing fractions given by

$$\chi = m_2 \ / \ (m_1 \ + m_2) \tag{6}$$

where m_1 is the mass of air from above the EIL in the mixture and m_2 is the mass of cloudy air in the mixture. This analysis has been used frequently [*Siems et al*., 1990; *Wang and Albrecht*, 1994; *Shao et al*., 1997; *Stevens*, 2002; *VanZanten and Duynkerke*, 2002; *de Roode and Wang*, 2007; *Mellado et al*., 2007; *Kurowski et al*., 2009; *Yamaguchi and Randall*, 2012; *Hill*, 2012; S. A. Hill et al., The entrainment interface layer of stratocumulus-toped boundary layers during POST, submitted to *Atmosphere Research*, 2013]. The analysis predicts in part the amount of negative buoyancy caused by LWC evaporation in mixtures of corresponding χ values. The values are calculated for POST Sc by noting that equation (5) can be rewritten to give $\chi = \delta q_t/\Delta q_t$ [*VanZanten and Duynkerke*, 2002] where δq_t is the local change of q_t in the EIL following mixing.

[52] Equations (16)–(20) in *Stevens* [2002] describing "saturated buoyancy perturbations" (no radiation effects included) are used along with the jumps listed in Table 1 to calculate the average maximum buoyancy change b^* between the unaffected cloud and the mixture in cloud holes, and to calculate the corresponding χ^* for each flight. The superscript asterisk indicates b and χ values representing the borderline

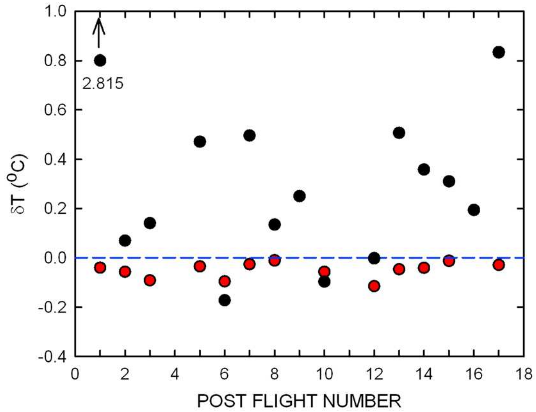

Figure 13. The temperature change (δT_p, black circles) predicted by mixture fraction analysis for POST flights, and the mean measured temperature change (δT_m, red circles) in cloud holes for POST flights (see text and Table 4).

between cloudy and cloud-free mixtures. The value of b^* can represent mixtures with either positive or negative buoyancy change with the latter predicting the largest cooling possible due to LWC evaporation. The buoyancy change is used to calculate the predicted temperature change δT_P that corresponds to b^* of the mixtures (see Table 4). Only flights TO6, TO10, and TO12 have predicted negative b^* and temperature changes (buoyancy reversal in holes) due to LWC evaporation in cloudy mixtures, in agreement with the CTEI and mixture fraction analysis results in the preceding sections. According to Table 4, all other POST flights show predicted average temperatures warmer than unaffected cloud top in mixtures between cloudy air and the free atmosphere above the EIL. Table 4 also lists the average measured temperature change δT_m between cloud holes and cloud unaffected by entrainment. Figure 13 plots both sets of temperature changes and illustrates the large differences between the predicted and measured temperature changes.

[53] Flights TO6, TO10, and TO12 are chosen for a closer look in the following, because the predicted buoyancy reversal for those flights suggests that LWC evaporation causes cooling in their entrained mixtures.

4.3. Cooled Cloud Holes

[54] Figure 14 shows portions of flights TO10 and TO12 where 50 Hz UFT-M temperature data are compared to the presence of cloud holes identified from the synchronized 50 Hz LWC data. The temperature record shows reduced values over small time intervals from a roughly constant background temperature. The correlation between the locations of reduced temperature and LWC holes is apparent. However, in Figure 14, some periods of reduced temperature (1) are not related to cloud holes, are partially filled with a cloud hole, and (3) are totally filled with a cloud hole. The lack of cloud holes in 1 and 2 indicates that the reduced temperature periods in Figure 14 can form without cooling due to LWC evaporation. The filled periods 3 show about the same cooling as 1 and 2 further suggesting a cooling effect in the reduced temperature periods is dominated by IR radiative cooling rather than by LWC evaporation.

[55] A similar conclusion results for TO6 which has the largest predicted buoyancy reversal. Figure 15 shows the measured maximum reduction of LWC′ in holes for TO6 as a function of the corresponding temperature δT_m. The data point at the end of the dashed line is the maximum δT_p value predicted by mixture fraction analysis. All measured data point should fall above the dashed line if cooling due to LWC evaporation plays a significant role. Instead, δT_m appears approximately independent of the depleted LWC′ in holes indicating a lack of significant cooling due to droplet evaporation. The analysis similar to Figure 15 is done for all flights; all show insignificant cooling due to evaporation and most show some warming especially for large values of −LWC′ that occur near cloud top. (For plots of δT_m versus LWC′ for other flights, see http://www.gerberscience.com/POSTdata/POSTdata.html)

[56] The results from TO6, TO10, TO13 support the earlier findings [*Gerber et al.*, 2002, 2005; *de Roode and Wang*, 2007] from DYCOMS and DYCOMS II that detrainment at Sc top cools and moistens the EIL until a near-buoyancy match takes place between the cloud and the EIL adjacent to cloud top. Radiative cooling near cloud top apparently destabilizes the air causing entrainment of the conditioned EIL mixture. The conditioning of the EIL is also a conclusion reached by *Yamaguchi and Randall* [2012] who noted

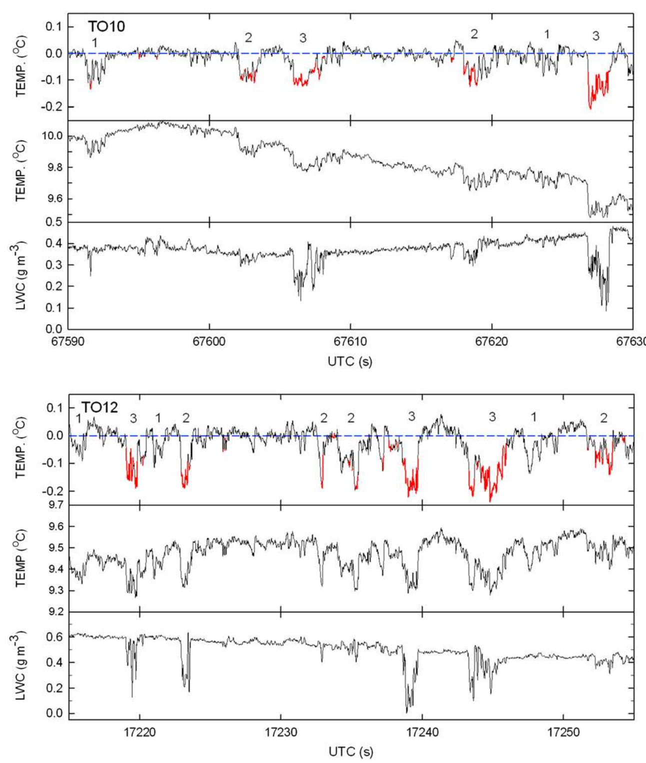

Figure 14. Fifty hertz data of expanded portions of flights TO10 and TO12 as a function of time showing the relationship between detrended UFT-M temperature (top plot, black) and the location of cloud holes (entrained parcels, red) identified by depleted liquid water content (LWC′) and the corresponding UFT-M temperature (middle plot) and LWC (bottom plot) data for each flight. Blue dashed lines estimate the background cloud temperature unaffected by entrainment. Number 1 indicates reduced temperature sections without LWC′, Number 2 sections have some LWC′, and Number 3 sections are filled with LWC′.

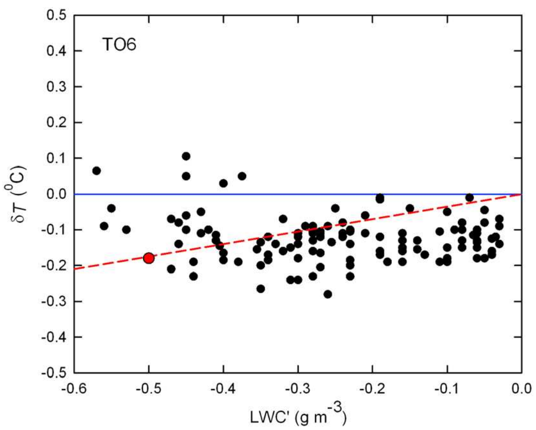

Figure 15. The temperature change δT_m in cloud holes (black circles) corresponding to the maximum value of depleted liquid water content LWC′ found in each hole for flight TO6. The red circle and dashed line indicate predictions from mixture fraction analysis for evaporative cooling (see text).

that radiative cooling and cooling due to LWC evaporation are of the same order of magnitude, where the significant LWC cooling occurs in the EIL. LES modeling by *Moeng et al*. [2005] also concludes that Sc evaporate at cloud top.

[57] The apparent lack of significant evaporative cooling in entrainment holes for POST Sc differs with how entrainment is looked at in earlier modeling where entrainment is enhanced when droplet concentration is larger (less "droplet sedimentation") causing greater radiative cooling and greater evaporative cooling in the holes [*Ackerman et al*., 2004; *Bretherton et al*., 2007; *Caldwell and Bretherton*, 2009]. The present results suggest instead that changes in droplet concentration for a given LWC should have a minimal effect on the entrainment rate, at least for the unbroken POST Sc. The role of larger values of LWC is to cause more evaporation in the EIL and to more efficiently reduce the potential energy of overlying warm and dry air causing enhanced entrainment in an indirect manner. Whether this indirect evaporative cooling is identical to hypothetical evaporative cooling in the holes and affects the buoyancy generation in the cloud the same way depends on detrainment and the behavior of the EIL which remain to be clarified. For typically large T jumps across the EIL, this indirect effect becomes minimal, because the EIL conditioning is dominated by the detrainment of sensible heat from the cloud. However, the evaporative cooling in the EIL becomes important for small temperature jumps. The effect of radiative cooling on droplet concentration and LWC changes also should be minimal, because the blackbody radiative behavior of unbroken Sc remains efficient despite such changes. Only the maximum radiative cooling at cloud top changes, whereas the radiative cooling rate, °C $\mathrm{h^{-1}\,m^{-3}}$, integrated over the cloud depth appears to remain the same [*Davies and Alves*, 1989]. High-resolution modeling near cloud top is required to resolve the effect of vertical radiative cooling that changes rapidly just below cloud top.

[58] All POST flights show evidence of mixing at cloud top suggesting that detrainment occurs for all. However, this does not mean that the temperature in all descending holes is a result of radiative cooling. Holes warmer than the adjacent unaffected cloud are also observed for flights such as TO3 and TO13 with strong shear and deep penetration of holes into the Sc. Such warm air entrainment is similar to the strong Sc shear case modeled by *Wang et al*. [2012] which concludes that the enhanced entrainment causes enhanced evaporation and negative buoyancy production but also reduces the positive buoyancy in the Sc.

[59] The described buoyancy-matching nature of entrainment leads to an explanation why CTEI does not cause breakup of Sc when the critical value of $k = 0.23$ is exceeded. Both the formulations for CTEI and mixture fraction analysis assume that cloud top mixes directly with the free atmosphere above the inversion. Since entrained parcels come from the conditioned EIL having undergone prior mixing, k values will be smaller than when cloud top mixes directly with the free atmosphere. Also, models [*Moeng et al*., 2005; *Wang et al*., 2008] and measurements [*Lenschow et al*., 2000; *de Roode and Wang*, 2007; *Katzwinkel et al*., 2011] including those for POST Sc [*Malinowski et al*., 2013] show that the separation between cloud top and the top of the inversion is continuous. Therefore, direct interaction of cloud top with the free atmosphere does not occur and the usual applications of k and χ do not apply. If the assumption is made that T and q_v are approximately inversely proportional in the EIL, then conditioned mixtures in the EIL will remain either nonbuoyant or buoyant with smaller values of k and b than such values predicted by the usual CTEI and mixture fraction analyses. The δT_p values in Figure 13 based on *Stevens* [2002] buoyancy equations for mixtures relate to the jump across the EIL without intermediate mixing by conditioning. Thus, those δT_p values are too large and should be much closer to the $\delta T = 0$°C line in Figure 13.

4.4. Effective Radius and Mixing

[60] The high-rate PVM data make it possible to estimate the changes in effective radius R_e of cloud droplets caused by entrainment and thus deduce the nature of the mixing mechanism termed either homogeneous or inhomogeneous mixing (see *Jensen et al*. [1985] for definitions of the mixing mechanisms). The PVM simultaneously measures LWC/PSA (particle surface area) which is proportional to R_e that is also approximately equal to the mean volume radius (r_v) when the droplet size spectrum is relatively narrow [*Martin et al*., 1994; *Gerber*, 1996; *Gerber et al*., 2008].

[61] Both R_e and r_v have been compared to LWC and droplet concentrations N to establish the mixing mechanism following entrainment [*Gerber*, 2000; *Gerber et al*., 2008; *Burnet and Brenguier*, 2007; *Lehmann et al*., 2009; *Lu et al*., 2011] Independence of R_e or r_v on changes in LWC or N is thought to reflect the inhomogeneous mixing mechanism; whereas changes in all parameters reflect homogeneous mixing. *Burnet and Brenguier* [2007] conclude that inhomogeneous mixing occurs in maritime Sc from DYCOMS II, and *Lu et al*. [2011] found the same mechanism dominating warm continental Sc, although they also observed an instance of homogenous mixing.

[62] Figure 16 shows the relationship between LWC and R_e with an in-cloud resolution of 20 cm for first ~10 s of penetration into TO3, TO10, and TO13. All plots in Figure 16 show nearly constant values of R_e while LWC shows large changes, suggesting that mixing is of inhomogeneous nature. Some portions of the data for TO3 show reductions in R_e,

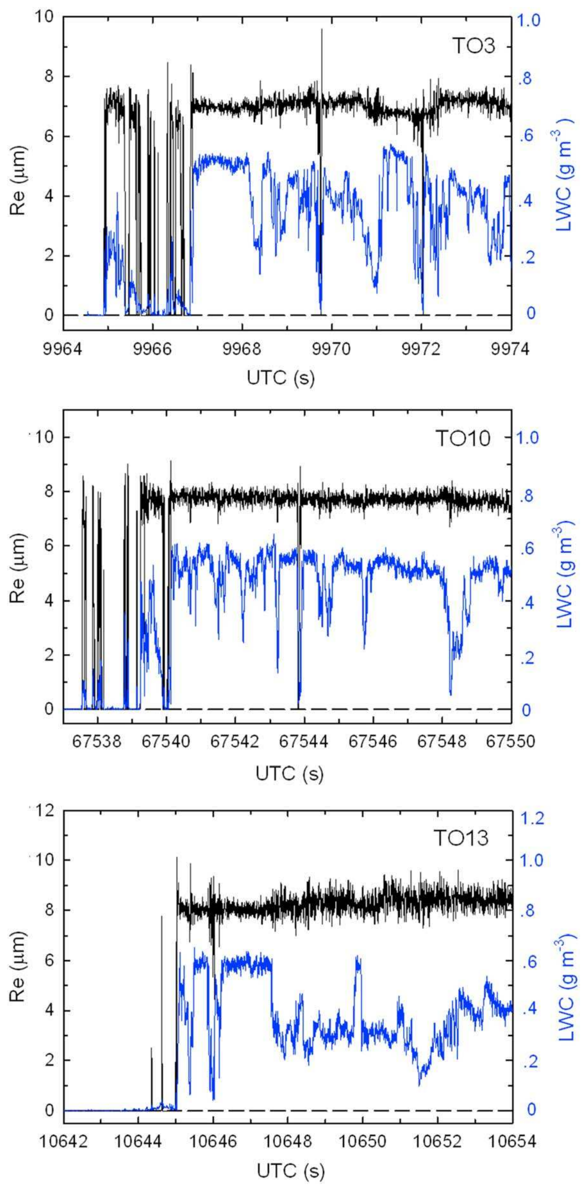

Figure 16. Effective radius R_e and LWC for the first ~10 s of a descent into Sc on flights TO3, TO10, and TO13 using 20 cm resolution data.

examples are at UTC = 9969.7 s and 9972 s. About 10% of the TO3 data show such reductions which occur when the value of LWC is smallest, suggesting that some homogenous mixing is taking place. Both TO10 and TO13 show a lesser percentage of reduced R_e. *Malinowski et al*. [2013] describe a result for TO13 where significant changes of the droplet spectrum are measured; however, the changes occur deeper in the cloud where entrained warm air is mixing with the rest of the cloud.

[63] The analysis of R_e versus LWC for POST flights indicates that inhomogenous-type mixing dominates in keeping with the conclusion reached by *Burnet and Brenguier* [2007] for DYCOMS II Sc. However, if the entrained air is pre-preconditioned and at nearly the same T and q_v as the cloud near cloud top, as shown for TO3, TO10, and TO13, it is not possible to distinguish between inhomogeneous and homogeneous mixing as also noted by *Burnet and Brenguier* [2007].

5. Conclusions

[64] The main impression left by this analysis of POST flights in unbroken Sc is their large variability: Sc cloud top rises or lowers for both day and night flights, the inversion is often sloped, strong shear at cloud top causes strong mixing in some Sc, and the application of classical entrainment rate formulation is questionable for most Sc. The complexities are likely related to the location of the POST flights off the coast of California near Monterey where an earlier aircraft Sc field study [*Wakefield and Schubert*, 1976; *Brost et al*., 1982a] in the same general area found offshore Sc affected by strong sea surface temperature gradients and by the continent causing the baroclinic nature of the atmosphere associated with wind shear and sloped inversions.

[65] The main emphasis of the present analysis is to estimate the entrainment velocity w_e into POST Sc in order to permit comparisons with model predictions. An unexpected complexity arises in this analysis because entrained parcels, termed cloud holes where droplet evaporation and/or dilution create narrow regions of reduced liquid water content, are observed to descend as well as ascend. This causes the net value of the entrainment flux F_e as well as w_e to be unrealistically close to zero for some Sc, even though these Sc are filled with holes. In order to deal with this situation, the assumption is made that due to turbulence and mixing at cloud top ascending holes just below cloud top are lost by moving move up through the cloud top interface and evaporating their LWC causing cooling and moistening of the EIL. All F_e values for ascending holes are given positive values in equation (2) for the formulation of equation (2) to be consistent with this assumption. The effect is to produce more realistic values of F_e at cloud top as well as more realistic values of w_e that now reflect both entrainment and detrainment at cloud top. The uncertainty in the calculated values of w_e is increased since detrainment is not directly measured in this approach.

[66] The value of w_e estimated for all flights is given by the ratio $F_e/\Delta q_t$ where F_e is the entrainment mass flux and Δq_t is the total water jump between cloud top and the top of the inversion. The largest source of uncertainty in w_e is choosing the value of Δq_t that for some flights requires subjectivity. Also, small values of Δq_t cause large uncertainty in w_e. The measurement of F_e is often more robust than the measurement of w_e and is useful for comparison with model predictions.

[67] The analysis of individual cloud holes permitted by the colocation within 0.5 m on the Twin Otter aircraft of the high-rate-temperature (UFT-M) and liquid-water-content (PVM) probes leads to the following conclusions: Measurements indirectly lead to the conclusion that cloud holes cooler than the adjacent cloud unaffected by entrainment are a result of radiative cooling and are not due to LWC evaporation which appears minimal in the holes. Such holes are observed in all flights. This conclusion is reached because of the presence of cooled parcels near cloud top that do not contain reduced LWC and of the reduction of LWC in cloud holes that does not lead to increased cooling in the holes. These observations strengthen the earlier conclusion that detrainment conditions the lower part of the EIL so that the moisture and temperature of entrainment air are nearly the same as in the cloud at cloud

top. However, the observations also show other holes warmer than the adjacent cloud and show that these holes that can penetrate deep into the cloud causing droplet evaporation and Sc dissipation such as for Sc from TO3. Sc with strong shear and resulting turbulence and mixing causes the largest number of warm holes.

[68] Observations show Sc cloud top rarely contacting the top of the EIL and show entrained parcels preconditioned by detrainment in the lower part of the EIL which lead to the conclusion that the usual predictions of CTEI and buoyancy reversal dealing with jumps across the entire EIL are quantitatively incorrect.

[69] Some Sc show entrainment behavior where warm holes are rare and the holes are cool and descend in keeping with classical mixed layer theory, similar to one Sc case observed during DYCOMS II [*Gerber et al*., 2005]. However, most POST Sc show non-classical behavior with strong mixing in-cloud and chaotic motion of the holes. The location of DYCOMS II Sc study, far from the continent, was chosen partly to avoid environmental complexities such as found for the POST Sc. Another look at the DYCOMS II Sc is warranted to see if their entrainment process is classical for all Sc.

[70] The conditional sampling of the holes in the POST Sc also produces information relating the length of the holes to F_e as observed from the Twin Otter aircraft. The distribution of hole lengths versus F_e is lognormal for all flights, with the contribution to F_e negligible for lengths greater than a few hundred meters. To capture 90% of F_e, all lengths greater than ~5 m should be measured or modeled.

[71] The high-rate PVM data also produce measurements of effective radius (R_e) that are used to determine the mixing mechanism following entrainment. A comparison of R_e and LWC near cloud top for three POST flights shows mostly constant values of R_e, while LWC has large variations. This leads to the conclusion that inhomogeneous-type mixing dominates during entrainment at cloud top during which droplet concentrations are diluted and the relative droplet spectra remain the same in keeping with earlier conclusions reached for DYCOMS II Sc. However, in POST Sc, such for TO13 with significant warm air entrainment, droplet sizes can change [*Malinowski et al*., 2013] suggesting the presence of homogeneous mixing.

[72] The 17 POST flights generated a large database limiting the present study's close look to only three flights. While the calculated w_e values for all flights show some trends with respect to other measured variables on the aircraft, it was judged premature to attempt a new parameterization of w_e. Clearly, more analysis of the POST data is desirable, as are comparisons with high-resolution LES models. The quasi-Lagrangian flight patterns used during POST proved to be useful but were of relatively short duration (~3 h.). Another field study of Sc is recommended given that the technology for measuring entrainment in Sc from aircraft appears mature and that longer flight durations with more than one aircraft are desired.

[73] **Acknowledgments.** POST was a collaborative effort involving about two dozen participants. H. Gerber gives special thanks to the following individuals: The Twin Otter chief scientist Haf Jonsson and his CIRPAS associates Roy Woods, Jesus Galvan, and Bob Bluth provided a superior environment making possible the successful running of the POST field campaign. Mike Hubbell, the Twin Otter pilot, flew the aircraft in an exacting manner to meet the PIs flight pattern demands including the quasi-Lagrangian patterns. Tak Yamaguchi, Qing Wang, Steven Krueger, Rob Wood, and Anthony Bucholtz took turns flying on the Twin Otter as flight scientists. Dion Rossiter put together the flight reports. Stuart Beaton brought the new NCAR Lyman-alpha hygrometer for deployment on the aircraft. Wojciech Kumala was responsible for the construction and maintenance of the University of Warsaw ultrafast temperature probe without which POST would not have succeeded. Janine Goldstein made the PIs' data available on the POST Web site which was constructed by RAF/NCAR. NSF supported H. Gerber, G. Frick, and S. Malinowski (ATM-0735121, AGS-1020445), D. Khelif (ATM-0734323), and S. Krueger (ATM-0735118). The Office of Naval Research and the Naval Postgraduate School supported in part the deployment of the Twin Otter aircraft.

References

Ackerman, A. S., M. Kirkpatrick, D. Stevens, and O. Toon (2004), The impact of humidity above stratiform clouds on indirect aerosol climate forcing, *Nature*, *432*, 1014–1017, doi:10.1038/nature03174.

Albrecht, B. A., R. S. Penc, and W. H. Schubert (1985), An observational study of cloud topped mixed layers, *J. Atmos. Sci.*, *42*, 800–822.

Albrecht, B. A., D. A. Randall, and S. Nicholls (1988), Observations of marine stratocumulus during FIRE, *Bull. Am. Meteorol. Soc.*, *69*, 618–626.

Bretherton, C. S., T. Uttal, C. W. Fairall, S. E. Yuter, R. A. Weller, D. Baumgardner, K. Comstock, and R. Wood (2004), The EPIC 2001 stratocumulus study, *Bull. Am. Meteorol. Soc.*, *85*, 967–977.

Bretherton, C. S., P. Blossey, and J. Uchida (2007), Cloud droplet sedimentation, entrainment efficiency, and subtropical stratocumulus albedo, *Geophys. Res. Lett.*, *34*, L03813, doi:10.1029/2006GL027648.

Brost, R. A., D. H. Lenschow, and J. C. Wyngaard (1982a), Marine stratocumulus layers. Part I: Mean conditions, *J. Atmos. Sci.*, *39*, 800–817.

Brost, R. A., J. C. Wyngaard, and D. H. Lenschow (1982b), Marine stratocumulus layers. Part II: Turbulence budgets, *J. Atmos. Sci.*, *39*, 818–836.

Burnet, F., and J.-L. Brenguier (2007), Observational study of the entrainment-mixing process in warm convective clouds, *J. Atmos. Sci.*, *64*, 1995–2011.

Caldwell, P., and C. S. Bretherton (2009), Large eddy simulation of the diurnal cycle in Southeast Pacific stratocumulus, *J. Atmos. Sci.*, *66*, 432–449.

Carman, J. K., D. L. Rossiter, D. Khelif, H. H. Jonsson, I. C. Faloona, and P. Y. Chuang (2012), Observational constraints on entrainment and the entrainment interface layer in stratocumulus, *Atmos. Chem. Phys.*, *12*, 11,135–11,152.

Chaughey, S. J., B. A. Crease, and W. T. Roach (1982), A field study of nocturnal stratocumulus: II. Turbulence structure and entrainment, *Quart. J. R. Meteor. Soc.*, *108*, 125–144.

Davies, R., and A. R. Alves (1989), Flux divergence of thermal radiation within stratiform clouds, *J. Geophys. Res.*, *94*(D13), 16,277–16,286.

Deardorff, P. D. (1980), Cloud-top entrainment instability, *J. Atmos. Sci.*, *37*, 131–147.

de Roode, S. R., and Q. Wang (2007), Do stratocumulus clouds detrain? FIRE I data re-visited, *Boundary-Layer Meteor.*, *122*, 479–491.

Duynkerke, P. G. (1993), The stability of cloud top with respect to entrainment: Amendment of the theory of cloud top entrainment instability, *J. Atmos. Sci.*, *50*, 495–502.

Faloona, I., D. H. Lenschow, T. Campos, B. Stevens, M. C. VanZanten, B. Blomquist, D. Thornton, A. Bandy, and H. Gerber (2005), Observations of entrainment in Eastern Pacific marine stratocumulus using three conserved scalars, *J. Atmos. Sci.*, *62*, 3268–3285.

Gerber, H. (1980), A saturation hygrometer for the measurement of relative humidity between 95% and 105%, *J. Appl. Meteorol.*, *19*, 1196–1208.

Gerber, H. (1986), Tethered balloon measurements at San Nicolas Island (Oct. 1984): Instrumentation data summary, preliminary data interpretation. Naval Research Laboratory Report 8972, 77 pp.

Gerber, H. (1991), Supersaturation and droplet spectral evolution in fog, *J. Atmos. Sci.*, *48*, 2569–2588.

Gerber, H. (1994), Hygrometer for measurement of relative humidity in clouds. *Final Report*, National Science Foundation Grant No. 9261243, pp. 19.

Gerber, H. (1996), Microphysics of marine stratocumulus clouds with two drizzle modes, *J. Atmos. Sci.*, *53*, 1649–1662.

Gerber, H. (2000), Structure of small cumulus clouds. *Proc. 13th Intern. Conf. Clouds and Precip*., Reno, NV, 14–18 Aug., 2000, 105–105.

Gerber, H., S. Chang, and T. Holt (1989), Evolution of a boundary-layer jet, *J. Atmos. Sci.*, *46*, 1312–1326.

Gerber, H., B. G. Arends, and A. S. Ackerman (1994), New microphysics sensor for aircraft use, *Atm. Res.*, *31*, 235–252.

Gerber, H., S. P. Malinowski, J.-L. Brenguir, and F. Burnet (2002), On the entrainment process in stratocumulus clouds. *11th Conf. On Cloud Physics*, Ogden, UT; Amer. Meteor. Soc., paper 7.6, https://ams.confex.com/ams/11AR11CP/webprogram/Paper44890.html.

Gerber, H., S. P. Malinowski, J.-L. Brenguier, and F. Burnet (2005), Holes and entrainment in stratocumulus, *J. Atmos. Sci.*, *62*, 443–459.

Gerber, H., G. M. Frick, J. B. Jensen, and J. G. Hudson (2008), Entrainment, mixing, and microphysics in trade-wind cumulus, *J. Meteorol. Soc. Japan*, *86A*, 87–106.

Gerber, H., G. Frick, S. P. Malinowski, W. Kumula, and S. Krueger (2010), POST—A new look at stratocumulus. *13th Conf. On Cloud Physics*, Portland, OR, 2010, Amer. Meteor. Soc., https://ams.confex.com/ams/13CldPhy13AtRad/webprogram/Paper170431.html.

Haman, K. E., S. P. Malinowski, B. Strus, R. Busen, and A. Stefko (2001), Two new types of ultra-fast aircraft thermometer, *J. Atmos. Oceanic Technol.*, *18*, 117–134.

Haman, K. E., S. P. Malinowski, M. J. Kurowski, H. Gerber, and J.-L. Brenguier (2007), Small scale mixing processes at the top of a marine stratocumulus—A case study, *Quart. J. R. Meteor. Soc.*, *133*, 213–226, doi:10.1002/qj.5.

Hanson, H. P. (1984), On mixed-layer modeling of the stratocumulus topped marine boundary layer, *J. Atmos. Sci.*, *41*, 1226–1234.

Hill, S. A. (2012), The entrainment interface layer of stratocumulus-topped boundary layer during the POST field campaign. Master's Thesis, May 2012, Dept. Atm. Sci., University of Utah.

Jensen, J. B., P. H. Austin, M. B. Baker, and A. M. Blyth (1985), Turbulent mixing, spectral evolution and dynamics in a warm cumulus cloud, *J. Atmos. Sci.*, *42*, 173–192.

Katzwinkel, J., H. Siebert, and R. A. Shaw (2011), Observations of a self-limiting, shear-induced turbulent inversion layer above marine stratocumulus, *Boundary Layer Meteorol.*, *145*, 131–143.

Khalsa, S. J. S. (1993), Direct sampling of entrainment events in a marine stratocumulus layer, *J. Atmos. Sci.*, *50*, 1734–1750.

Khelif, D., S. P. Burns, and C. A. Friehe (1999), Improved wind measurements on research aircraft, *J. Atmos. Oceanic Technol.*, *16*, 860–875.

Khelif, D., C. A. Friehe, H. Jonsson, Q. Wang, and J. Kalogiros (2005), Wintertime boundary-layer structure and air-sea interaction over the Japan/East Sea, *Deep Sea Res., Part II*, *52*, 1525–1546.

Korolev, A. V., and I. P. Mazin (1993), Zones of increased and decreased droplet concentration in stratiform cloud, *J. Appl. Meteorol.*, *32*, 760–773.

Kuo, H. C., and W. H. Schubert (1988), Stability of cloud-topped layers, *Quart. J. R. Meteor. Soc.*, *114*, 887–916.

Kumula, W., K. E. Haman, M. Kopec, and M. K. Malinowski (2013), Ultrafast thermometer UFT-M: High resolution temperature measurements during Physics of Stratocumulus To [POST], *Atmos. Meas. Tech.*, http://www.atmos-meas-tech.net/6/2043/amt-6-2043-2013.html.

Kurowski, M. J., S. P. Malinowski, and W. W. Grabowski (2009), Numerical investigation of entrainment and transport within stratocumulus-topped boundary layer, *Quart. J. R. Meteor. Soc.*, *135*, 77–92, doi:10.1002/qj.354.

Lehmann, K., H. Siebert, and R. A. Shaw (2009), Homogenous and inhomogeneous mixing in cumulus clouds: Dependence on local turbulence structure, *J. Atmos. Sci.*, *66b*, 3641–3659, doi:10.1175/2009JAS3012.1.

Lenschow, D. H., I. Paluch, A. Bandy, R. Pearson Jr., S. Kawa, C. Weaver, B. Huebert, J. Kay, D. Thornton, and A. Driedger (1988), Dynamics and chemistry of marine stratocumulus (DYCOMS) experiment, *Bull. Am. Meteorol. Soc.*, *69*, 1058–1067.

Lenschow, D. H., M. Zhou, X. Zeng, L. Chen, and X. Xu (2000), Measurements of fine-scale structure at the top of marine stratocumulus, *Boundary-Layer Meteor.*, *97*, 331–357.

Lilly, D. K. (1968), Models of cloud-topped mixed layers under a strong inversion, *Quart. J. R. Meteor. Soc.*, *94*, 292–309.

Lu, C., Y. Liu, and S. Niu (2011), Examination of turbulent entrainment-mixing mechanism using a combined approach. *J. Geophys. Res.*, *116*, D20207, doi:10.1029/2011JD015944.

MacVean, M. K., and J. P. Mason (1990), Cloud-top entrainment instability through small-scale mixing and its parameterization in numerical models, *J. Atmos. Sci.*, *47*, 1012–1030.

Malinowski, S. P., K. E. Haman, M. K. Kopec, W. Kumula, H. Gerber, and S. K. Krueger (2010), Small scale variability of temperature and LWC at stratocumulus top, *13th Conf. on Cloud Phys*., Portland, OR. Amer. Meteor. Soc., http://ams.confex.com/ams/13CldPhy13AtRad/webprogram/Paper170832.html.

Malinowski, S. P., K. E. Haman, W. Kumula, and H. Gerber (2011), Small-scale turbulent mixing at stratocumulus top observed by means of high resolution airborne temperature and LWC measurements, *J. Phys. Conf. Ser.*, *318*, doi:10.1088/1742-6596/318/7/072013.

Malinowski, S. P., et al. (2013), Physics of Stratocumulus Top (POST): Turbulent mixing across capping inversion, *Atmos. Chem. Phys. Discuss.*, *13*, 15,233–15,269, doi:10.5194/acpd-13-15233-2013.

Martin, G. M., D. W. Johnson, and A. Spice (1994), The measurement and parameterization of effective radius of droplets in warm stratocumulus clouds, *J. Atmos. Sci.*, *51*, 1823–1842.

Mellado, J. P., B. Stevens, H. Schmidt, and N. Peters (2007), Buoyancy reversal in cloud-top mixing layers, *Quart. J. R. Meteor. Soc.*, *135*, 963–978, doi:10.1002/qj.417.

Moeng, C.-H., B. Stevens, and P. P. Sullivan (2005), Where is the interface of the stratocumulus-topped PBL?, *J. Atmos. Sci.*, *62*, 2626–2631.

Nicholls, S. (1989), The structure of radiatively driven convection in stratocumulus, *Quart. J. R. Meteor. Soc.*, *115*, 487–511.

Nicholls, S., and J. D. Turton (1986), An observational study of the structure of stratiform cloud sheets: Part II. Entrainment, *Quart. J. R. Meteor. Soc.*, *112*, 461–480.

Randall, D. A. (1980), Conditional instability of the first kind up-side-down, *J. Atmos. Sci.*, *37*, 125–130.

Roach, W. T., R. Brown, S. J. Caughey, B. A. Crease, and A. Slingo (1982), A field study of nocturnal stratocumulus. 1. Mean structure and budgets, *Quart. J. R. Meteor. Soc.*, *108*, 103–123.

Shao, Q., D. A. Randall, C. H. Moeng, and R. E. Dickinson (1997), A method to determine the amounts of cloud-top radiative and evaporative cooling in a stratocumulus-topped boundary layer, *Quart. J. R. Meteor. Soc.*, *123*, 2187–2213.

Siems, S. T., C. S.,. Bretherton, M. B. Baker, S. Shy, and R. T. Breidenthal (1990), Buoyancy reversal and cloud-top entrainment instability, *Quart. J. R. Meteor. Soc.*, *116*, 705–739.

Stevens, B. (2002), Entrainment in stratocumulus toped mixed layers, *Quart. J. R. Meteor. Soc.*, *128*, 2663–2690.

Stevens, B., et al. (2003a), Dynamics and chemistry of marine stratocumulus—DYCOMS II, *Bull. Am. Meteorol. Soc.*, *84*, 579–593.

Stevens, B., et al. (2003b), On entrainment rates in nocturnal marine stratocumulus, *Quart. J. R. Meteor. Soc.*, *129*, 3469–3493.

Sundararajan, M., and M. Tjernstrom (2000), Observations and simulations of a non-stationary coastal atmospheric boundary layer, *Quart. J. R. Meteorol. Soc.*, *126*, 445–476, part B.

VanZanten, M. C., and P. G. Duynkerke (2002), Radiative and evaporative cooling in the entrainment zone of stratocumulus—The role of longwave radiative cooling above cloud top, *Boundary-Layer Meteor.*, *102*, 253–280.

Wakefield, J. S., and W. H. Schubert (1976), Design of execution of the marine stratocumulus experiment. *Atmos. Sci. Paper No. 256*, Dept. of Atmos. Sci., Colorado State University, Ft. Collins, CO.

Wang, Q. (2009), POST data initial analyses. POST Science and Data Workshop (5–6 Feb., 2009), http://www.eol.ucar.edu/projects/post.

Wang, Q., and B. A. Albrecht (1994), Observations of cloud-top entrainment in marine stratocumulus clouds, *J. Atmos. Sci.*, *51*, 1530–1547.

Wang, Q., and D. H. Lenschow (1995), An observational study of the role of penetrating cumulus in a marine stratocumulus-topped boundary layer, *J. Atmos. Sci.*, *52*, 2778–2787.

Wang, S., J.-C. Golaz, and Q. Wang (2008), Effect of intense wind shear across the inversion on stratocumulus, *Geophys. Res. Lett.*, *35*, L15814, doi:10.1029/2008GL033865.

Wang, S., X. Zheng, and Q. Jiang (2012), Strongly sheared stratocumulus: An observationally based large-eddy simulation study, *Atmos. Chem. Phys.*, *12*, 5223–5235.

Wood, R. (2012), Stratocumulus clouds, *Mon. Weather Rev.*, *140*, 2373–2423.

Wood, R., and C. S. Bretherton (2004), Boundary layer depth, entrainment, and decoupling in the cloud-capped subtropical and tropical marine boundary layer, *J. Clim.*, *17*, 3576–3588.

Wood, R., et al. (2011), The VAMOS Ocean-Cloud-Atmosphere-Land Study Regional Experiment (VOCALS-REx): Goals, platforms, and field operations, *Atmos. Chem. Phys.*, *11*, 627–654.

Yamaguchi, T., and D. A. Randall (2012), Cooling of entrained parcels in a large-eddy simulation, *J. Atmos. Sci.*, *69*, 1118–1136, doi:10.1175/JAS-D-11-080.1.